Spin crossover and high-spin state in Fe(II) anionic polymorphs based on tripodal ligands

Emmelyne Cuza, Cle Donacier Mekuimemba, Nathalie Cosquer, Françoise Conan, Sébastien Pillet, Guillaume Chastanet, Smail Triki

Spin Crossover and High-Spin State in Fe(II) Anionic Polymorphs Based on Tripodal Ligands

Emmelyne Cuza, Cle Donacier Mekuimemba, Nathalie Cosquer, Françoise Conan, Sébastien Pillet, Guillaume Chastanet, Smail Triki*

ABSTRACT: Two new mononuclear Fe(II) polymorphs, $[(C_2H_5)_4N]_2[Fe(py_3C\text{-}OEt)(NCS)_3]_2$ (**1**) and $[(C_2H_5)_4N][Fe(py_3C\text{-}OEt)(NCS)_3]$ (**2**) (py_3C-OEt = tris(pyridin-2-yl)ethoxymethane) have been synthesized and characterized by single crystal X-ray diffraction, by magnetic and photomagnetic measurements, and by detailed variable temperature infrared spectroscopy. The molecular structure, in both complexes, is composed by the same anionic $[Fe(py_3C\text{-}OEt)(NCS)_3]^-$ complex (two units for **1**, and one unit for **2**) generated by a coordination, to the Fe(II) metal centre, of one tridentate py_3C-OEt tripodal ligand and three terminal κN-SCN co-ligands. Magnetic studies revealed that polymorph **2** displays high spin (*HS*) state in the whole studied temperature range (300-10 K), while complex **1** exhibits an abrupt and complete spin crossover (*SCO*) transition at *ca.* 132.3 K and for which the structural characterizations, performed at 295 and 100 K, show a strong modification, resulting from the thermal evolutions of the Fe-N bond lengths and of the distortion parameters (∑ and Θ) of the FeN_6 coordination sphere, in agreement with the presence of *HS* and *LS* states at 295 and 100 K, respectively. This thermal transition has been also confirmed by the thermal evolution of the maximum absorbance for ν(NCS) vibrational bands recorded in the temperature range 200-10K. In **1** the signature of a metastable photo-induced *HS* state has been observed using photo-magnetic and photo-infrared spectroscopy, leading to a similar *T(LIESST)* relaxation temperature (*LIESST* = Light-Induced Excited Spin-State Trapping) of 70 K.

■ INTRODUCTION

Among systems exhibiting switchable behaviors, spin crossover (*SCO*) materials are undeniably the most studied systems during the last few years, in view of their many potential applications, in particular for the development of new generations of sensors,[1-6] Organic Light-Emitting Diode (OLED),[7] displays[8-11] and memory devices.[11-15] *SCO* phenomenon can occur in molecular complexes for which the metal ion displays appropriate electronic configuration ($3d^4$-$3d^7$), that allows spin state change between the high spin (*HS*) and low spin (*LS*) states when the metal complex is subjected to external perturbation (eg. temperature, pressure or light irradiation). Even if systems based on Co^{II},[16-20] Mn^{III} [21-23] and Fe^{III} [24-36] are increasingly being investigated in the last few years thanks to considerable synthetic efforts, those based on the Fe(II) ion (d^6 electronic configuration) are, by far, the most reported systems.[37-59] However, while *SCO* complexes are, in their great majority, either cationic or neutral; the few *SCO* anionic systems reported up today are, to the best of our knowledge, restricted to Fe(III)[27-36] and Fe(II)[45-46,54-59] metal ions. Such anionic complexes are, however, essential for the design of multifunctional materials such as fluorescent or conducting switchable materials,[6,60] since they could allow, through appropriate metathesis syntheses, the possibility to introduce functional cations such as fluorescent cations or tetrathiafulvalene (TTF) derivatives electron-donor molecules.

For the Fe(II) complexes, only three different series have been investigated. The first one, $[Fe^{II}H_3L^{Me}][Fe^{II}L]X$ (X^- = AsF_6^-, BF_4^-, ClO_4^-, PF_6^-, SbF_6^-), reported by Tuchagues et al. in 2003, is based on the neutral H_3L^{Me} and on the deprotonated $(L^{Me})^{3-}$ hexadentate ligands, which was characterized as supramolecular 2D-array comprising *SCO* cationic ($[Fe^{II}H_3L^{Me}]^{2+}$) and anionic ($[Fe^{III}L^{Me}]^-$) complexes (see scheme 1a).[45] The second system consists on $[Fe^{II}_3(\mu\text{-}L)_6(H_2O)_6]^{6-}$ discrete trinuclear anionic units, based on substituted triazole (L^{2-}) anionic ligand (see scheme 1b),[46] that display a *HS-HS-HS* to *HS-LS-HS* transition above room temperature and an unexpected large hysteresis loop (> 85 K) in respect to the parent trinuclear neutral complexes well-known for their gradual *SCO* behavior without any significant cooperative effects.[47-53] For the last

series, the first Fe(II) SCO anionic complex, described in 2012, consists in the mononuclear $[Fe(py_4C)(NCS)_3]^-$ complex based on the rigid tripodal tetrakis(2-pyridyl)methane (py_4C) ligand (see schemes 1c, R = py).[54] This complex, of chemical formula $[Fe(py_4C)_2][Fe(py_4C)(NCS)_3]_2$, is composed from one *LS* complex cation, $[Fe(py_4C)_2]^{2+}$, and from two $[Fe((py_4C)(NCS)_3)]^-$ SCO complexes (see scheme 1d). Since then, this series has been enriched by other parent examples of general formula $[Me_4N][Fe(py_3C\text{-}R)(NCS)_3]$ (see schemes 1c, R = OH, CH_3, and -*n*-$C_{18}H_{37}$)[55-58] among which the $[Me_4N][Fe(py_3C\text{-}OH)(NCS)_3]\cdot(H_2O)$ complex exhibiting an abrupt hysteretic behavior with a relatively important heating-rate dependence.[55-56]

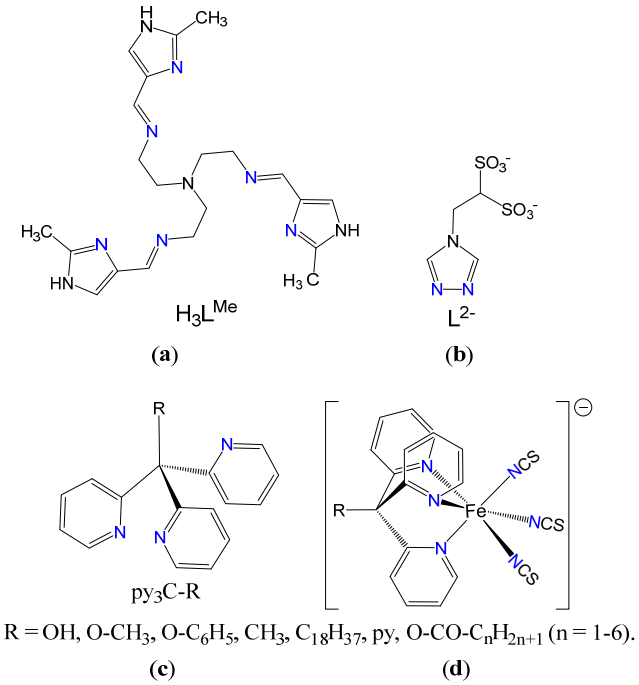

Scheme 1. Principal ligands used for the design of Fe(II) SCO anionic complexes: (**a**) tris-(2-(((2-methylimidazol-4-yl)methylidene)amino)ethyl)amine (H_3L^{Me}); (**b**) 4-(1,2,4-triazol-4-yl)ethanedisulfonate (L^{2-}); (**c**) examples of tris-(2-pyridyl)methane (py_3C-R) tripodal ligands and their principal coordination mode (**d**). See also table S1 gathering all the SCO compounds based on the $[Fe(py_3C\text{-}R)(NCE)_3]^-$ (E = S, BH_3) SCO complexes.

More recently, with the objective to shed more light on the effect of the linear NCE^- (E = S, BH_3) ancillary co-ligands on the *SCO* characteristics such as the transition temperatures, some of us reported two isomorph complexes of general formula, $[Fe(py_3C\text{-}OEt)_2][Fe(py_3C\text{-}OEt)(NCE)_3]_2.2CH_3CN$ (NCE^- = NCS^-, $NCBH_3^-$),[59] containing similar tripodal ligand but for which the counter-ion corresponds to the low spin

$[Fe(py_3C\text{-}OEt)_2]^{2+}$ complex, almost similar to that observed for the $[Fe(py_4C)_2][Fe(py_4C)(NCS)_3]_2$.[54]

Ultimately, during the preparation of this manuscript, two new series of anionic *SCO* complexes, $(Me_4N)[Fe(py_3C\text{-}C_nH_{2n+1})(NCS)_3]$ (n = 1−7) and $(Me_4N)[Fe(py_3C\text{-}CO_2C_nH_{2n+1}]$ (n = 1−6), have been reported.[61] In this work, the authors showed a clear effect, on the transition temperatures, of the odd−even of the number of carbon atoms of the alkyl groups attached to the py_3C motif, for each series. Last but not least, other neutral parent complexes, involving similar tridentate ligands and thiocyanato co-ligand, but acting as a μ-κN:κS-SCN bridging co-ligand, have also been investigated: this concerns the two dinuclear complexes $[\{Fe(py_3C\text{-}OH)(NCS)(\mu\text{-}NCS)\}_2](PrOH)_2$ and $[\{Fe(py_3C\text{-}OC_6H_5)(NCS)(\mu\text{-}NCS)\}_2]$ exhibiting *SCO* behavior and ferromagnetic interactions, respectively, despite their almost similar molecular structures.[62-63] This intriguing observation has been elucidated by magneto-structural studies which suggested that the *SCO* is favored by short Fe^{II}-N distances between the metal ion and the three nitrogen atoms of the tripodal ligand, and by relatively linear Fe-N-C(S) angles that promote a stronger ligand field.[63] In the same time, with the objective to understand the effect of the R functional group of the py_3C-R tripodal ligand on the structural features and on *SCO* behavior, we have prepared a new coordination polymer, $[\{Fe(py_3C\text{-}OMe)(NCS)(\mu\text{-}NCS)\}_n]$, exhibiting one dimensional (1-D) structure and an abrupt complete *SCO* transition with a transition temperature of 199 K.[64]

According to the study of two isomorph complexes, involving the two NCS^- and $NCBH_3^-$ ancillary co-ligands (see above),[59] that revealed significant effect of the linear anionic co-ligands on the transition temperatures, but without any significant influence on the cooperativity, we focused on the effect of the crystal packing on the SCO characteristics, with the objective to better control the cooperativity in such SCO systems. In this context, we report in the present work the syntheses, structural characterizations, magnetic properties and variable temperature infrared spectroscopy of the two polymorph complexes $[(C_2H_5)_4N]_2[Fe(py_3C\text{-}OEt)(NCS)_3]_2$ (**1**) and $[(C_2H_5)_4N][Fe(py_3C\text{-}OEt)(NCS)_3]$ (**2**) (py_3C-OEt = tris-(2-pyridyl)ethoxymethane),[65] as

the first anionic polymorphs for which one of them exhibits SCO behavior. Both complexes (**1** and **2**) have been prepared using the same reagents used for the synthesis of one of the two isomorphs noticed above ($[Fe(py_3C\text{-}OEt)_2][Fe(py_3C\text{-}OEt)(NCE)_3]_2.2CH_3CN$),[59] but in the present work, we have established appropriate synthesis protocol that clearly discriminates the nucleation and the crystal growth of each complex (see details in results discussion section).

■ EXPERIMENTAL SECTION

Materials and Physical Measurements. All starting reagents and solvents, and iron(II) salts were purchased (Sigma-Aldrich, Acros Organic, Cambridge Isotope Laboratories). The solvents have been dried under nitrogen using sodium and benzophenone for THF, CaH_2 for MeOH, BaO for DMF and sodium for EtOH. All the organic syntheses were performed under nitrogen atmosphere. The tris-(pyridin-2-yl)ethoxymethane (py_3C-OEt) ligand was prepared as previously described,[66-67] with slight modifications (see details in SI, and Figs S1-S10). Infrared spectra of the py_3C-OEt ligand and complexes have been performed at room temperature, in the 4000-400 cm^{-1} range, using a platinum ATR Vertex 70 BRUKER spectrometer. Temperature dependences of IR spectroscopy (including under irradiation at 10 K) were performed in the 2300-1900 cm^{-1} range, using a Nicolet 5700 FT-IR spectrometer with a DTGS KBr detector with KBr pellets, and a Vertex 70 BRUKER spectrometer with variable temperature cell holder (VT Cell Holder typer P/N GS21525). Photoexcitation in the IR measurement was carried out using a 505 nm LED (Thorlabs, model m505L3-C1) tuned to 40 mW (51 $mW.cm^{-2}$). The IR data have been qualitatively analysed in the form of absorbance (ABS) *vs.* wavenumber (in cm^{-1}). For the quantitative analysis and comparison with the thermo-magnetic and photo-magnetic measurements, the intensities of the *HS* vibration bands were represented as ABS *vs. T*, while the intensities of the *LS* vibration bands were represented as (1-ABS) *vs*. *T*. All NMR spectra (^1H et ^{13}C) spectra were performed using BRUKER DRX 300 MHz, Advance 400 MHz and Advance III HD 500 MHz equipment.

Syntheses of the complexes 1-2. $[(C_2H_5)_4N]_2[Fe(py_3C\text{-}OEt)(NCS)_3]_2$ (**1**)**:** tris-(pyridin-2-yl)ethoxymethane (23.0 mg, 0.079 mmol) and Fe(II) chloride salt (20.0 mg, 0.16 mmol) were dissolved in 5 mL of methanol, in presence of few mg of ascorbic acid. After 15 minutes of stirring at room temperature, was added acetonitrile solution (5mL) of $[(C_2H_5)_4N](NCS)$ salt (1.6 mmol). The resulting solution was then stirred for 5 minutes, filtered and directly placed at the -32 °C. Orange cubic single crystals of **1** were formed after three days. Anal. Calcd. (%) for $C_{29}H_{37}FeN_7OS_3$ (**1**): C, 53.4; H, 5.7; N; 15.0. Found (%): C, 53.7; H, 5.7; N, 14.8. $[(C_2H_5)_4N][Fe(py_3C\text{-}OEt)(NCS)_3]$ (**2**)**:** to a methanolic solution of iron (II) chloride tetrahydrate (21.8 mg, 0.11 mmol), and 0.62 mmol of $[(C_2H_5)_4N](NCS)$ was added a methanolic solution containing tris-(pyridin-2-yl)ethoxymethane (30.0 mg, 0.10 mmol). The resulting mixture was stirred for 30 minutes at 20 °C to give yellow microcrystalline powder (22 mg, yield: 33.8 %) after fast filtration. The resulting filtrate was placed in a large glass crystallizing dish to promote a faster evaporation, and was filtered only after five minutes of fast evaporation, to obtain single crystals of **2** as small yellow plates**.** Anal. Calcd. (%) for $C_{29}H_{37}FeN_7OS_3$ (**2**). C, 53.4; H, 5.7; N; 15.0. Found for the single crystals (%): C, 53.8; H, 5.6; N, 14.7; found for the polycrystalline powder (%): C, 53.7; H, 5.6; N, 14.6. As clearly depicted in Fig. S11, the infrared spectra of the single crystals of **1** and **2**, and of the polycrystalline powder of **2** are similar.

Magnetic and Photomagnetic Measurements. The magnetic studies were performed with a Quantum Design MPMS-XL-5 SQUID magnetometer in the 10-300 K temperature range with an applied magnetic field of 2 Tesla, using single crystals for compound **1** (m= 10.49mg, H = 10 kOe and scan rate = 0.4 $K.mn^{-1}$) and polycrystalline powder for compound **2** (m = 1.82 mg, H = 5 kOe, scan rate = 2 $K.mn^{-1}$). Photomagnetism for **1** and **2** were performed using a thin layer of sample whose thermal *SCO* curve was overlapped to the one obtained with the accurately weighted sample. Irradiations were applied through an optical fiber that connects a set of photodiodes to the SQUID sample holder. All the experiments were done using the standard measurement of the *T(LIESST)* temperature.[68] Magnetic susceptibility was

corrected for the diamagnetism on the basis of the corresponding chemical formula, using Pascal's tables.[69] (see SI for details).

X-ray Crystallography. The crystallographic studies were performed on single crystal and microcrystalline powder at various temperature. More details are provided in the Supplementary Information. Crystal data, structure refinement parameters, and selected bond lengths and bond angles are listed in Tables S2 and S3, respectively, while powder diffraction patterns are given in Figures S12 and S13.

■ RESULTS AND DISCUSSION

Synthesis. The py_3C-OEt ligand was prepared following the previously reported procedures[66-67] which have been slightly modified to increase the chemical yield. Syntheses of the Fe(II) single crystals of **1** and **2** were performed by reacting a methanolic solution of py_3C-OEt and iron (II) chloride with acetonitrile solution of $[(C_2H_5)_4N](NCS)$ salt. Slow evaporation at room temperature of the resulting solution gave a mixture of three different single crystals of different shapes, sizes and colors: the first type of crystals (prismatic red single crystals) corresponds to the compound of chemical formula $[Fe(py_3C\text{-}OEt)_2][Fe(py_3C\text{-}OEt)(NCS)_3]_2{\cdot}2CH_3CN$ (**3**), already reported very recently by some of us;[59] the second type consists of single crystals of yellow thin plates and corresponds to complex **2**; and the third one of cubic orange crystals corresponds to complex **1**.

To obtain each complex as pure single crystal, we have established appropriate synthesis protocols that discriminate the nucleation and the crystal growth of each complex separately (see details in experimental section). Single crystals of complex **1** were obtained when the final solution was quickly placed at -32 °C, to prevent the formation of single crystals of **2** and **3**; while the formation of single crystals of **2** requires fast evaporation in order to avoid the formation of complex **1**. In order to confirm the similarity between the single crystal and the polycrystalline powder of **2**, X-ray powder diffraction spectrum (XRPD) of the powder sample has been recorded at room temperature. The corresponding XRPD pattern depicted in Fig. S12 is almost

similar to that calculated from the single crystal structure. Although polymorph **1** was only obtained as single crystals, its corresponding X-ray powder diffraction pattern was performed (Fig. S13) to confirm absence of any crystalline impurities in the sample used for magnetic and spectroscopic studies. The absence of any non-crystalline impurities (or only very low fraction) in the powder sample of **2** was confirmed by infrared spectroscopy which showed that the spectrum recorded on the single crystal sample is similar to that observed for the corresponding polycrystalline powder (Fig. S11). However, as revealed by the magnetic data, this polycrystalline powder of **2** contains probably a fraction of *ca.* 5.5 % of polymorph **1,** which is not easily detected in the X-ray powder diffraction data (see details below).

Crystal Structures. Based on the magnetic data discussed below, the crystal structures have been determined at 295 K and at 100 K for compound **1,** and at 150 K and 90 K for compound **2.** The unit cell parameters, crystal and refinement data, and the relevant bond lengths and bond angles are given in Tables 1 and 2, respectively.

Table 1. X-ray data collection and refinement details for **1** and **2**.

Complex	**1**		**2**	
T / K	295	100	150	90
formula	$2(C_{29}H_{37}FeN_7OS_3)$		$C_{29}H_{37}FeN_7OS_3$	
Radiation	MoKα (λ = 0.71073 Å)		CuKα (λ = 1.54184 Å)	
M / g·mol^{-1}	1303.37		651.68	
Cryst. syst / SG	*Triclinic* / *P-1*		*Orthorhombic* / *Pca2$_1$*	
a / Å	10.5283(9)	10.3809(6)	15.7868(9)	15.6999(6)
b / Å	16.870(2)	16.6105(9)	14.5350(7)	14.4810(3)
c / Å	20.832(2)	20.183(2)	14.0806(6)	13.9943(4)
α / °	70.837(7)	70.108(5)	90	90
β / °	76.159(7)	75.477(5)	90	90
γ / °	90.385(7)	89.594(4)	90	90
V / Å^3	3378.8(5)	3156.3(3)	3231.0(3)	3181.6(2)
Z	2	2	4	4
ρ_{calcd} / g.cm^{-3}	1.281	1.371	1.340	1.361
[a]R_1 / [b]wR_2	0.0701 / 0.1491	0.0736 / 0.1632	0.0635 / 0.1896	0.0359 / 0.0905
[c]GooF	0.973	0.986	1.013	1.063
Flack parameter			0.015(9)	0.002(3)

[a]R1 = $\sum||Fo|-|Fc||/\sum|Fo|$; [b]wR2= $\{\sum[w(Fo^2-Fc^2)^2]/\sum[w(Fo^2)^2]\}^{1/2}$; [c]GooF= $\{\sum[w(Fo^2-Fc^2)^2]/(N\text{obs}-N\text{var})\}^{1/2}$

The following general structural descriptions will be restricted to the data collected at 295 K for **1** and at 150 K for **2**; the structural changes induced at low temperature (essentially for **1**) will be discussed in the following sections. Compounds **1**-**2** crystallise in triclinic (space group *P-1*) and in orthorhombic (space group *Pca2₁*) systems, respectively. The structure of **1** is built from two $[Fe(py_3C\text{-}OEt)(NCS)_3]^-$ symmetry independent anions centred on two Fe(II) ions (noted Fe1A and Fe1B) and two $[(C_2H_5)_4N]^+$ cations, all located on general positions (Fig. 1). The asymmetric unit of complex **2**, is only composed of one $[Fe(py_3C\text{-}OEt)(NCS)_3]^-$ anion centred on the Fe1 ion together with one $[(C_2H_5)_4N]^+$ cation, both located on general positions (Fig. 2). Such compositions led to the general crystallographic formula $[(C_2H_5)_4N]_2[Fe(py_3C\text{-}OEt)(NCS)_3]_2$ (**1**) and $[(C_2H_5)_4N][Fe(py_3C\text{-}OEt)(NCS)_3]$ (**2**), confirming that **1** and **2** are two mononuclear polymorphs.[65] In both polymorphs, the molecular structure is composed by the anionic $[Fe(py_3C\text{-}OEt)(NCS)_3]^-$ complex (two units Fe1A and Fe1B for **1**, and one unit Fe1 for **2**) involving a metal centre, one $py_3C\text{-}OEt$ chelating tripodal ligand and three terminal κN-SCN terminal co-ligands (Figs 1 and 2). All Fe(II) ions (Fe1A and Fe1B in **1**, Fe1 in **2**) are hexa-coordinated by six nitrogen atoms belonging to the three nitrogen atoms of the tripodal ligand, and from three $(NCS)^-$ co-ligands, in an approximate trigonal C_{3v} symmetry (or equivalently *3m* point group). Careful examination of the Fe-N bond lengths and N-Fe-N bonds angles (295 K for **1**, 150 K for **2**) reveals distorted FeN_6 octahedrons in both anionic complexes, caused in part, by the six Fe-N bond distances which are significantly different (Table 2): for each FeN_6 coordination environment (Fe1A, Fe1B for **1**, and Fe1 for **2**), the three Fe-N distances (N1A, N2A, N3A and N1B, N2B, N3B for **1**; N1, N2, N3 for **2**) arising from the coordination of NCS^- anions (2.078-2.126 Å), are systematically much shorter than the bond distances involving the nitrogen atoms (N4A, N5A, N6A and N4B, N5B, N6B for **1**; N4, N5, N6 for **2**) of the tridentate ligand (2.156-2.351 Å). Such distortions are accentuated by the values of bond angles that deviate considerably from the ideal values (*cis* angles: 78.3 to 99.0°, trans angles: 165.32-174.38°) which lead to high values of the distortion parameters (Σ = 53.4-56.7°, Θ = 107.7-148.7°).[70]

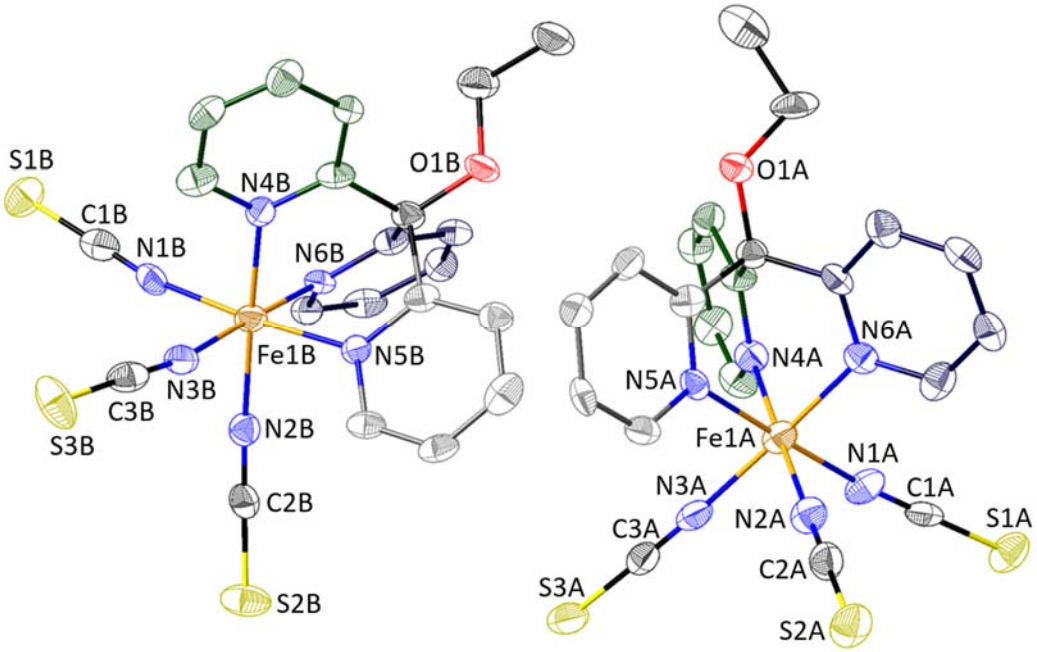

Figure 1. Molecular structure of the two anionic $[Fe(py_3C\text{-}OEt)(NCS)_3]^-$ complexes in **1** showing the FeN_6 distorted octahedrons.

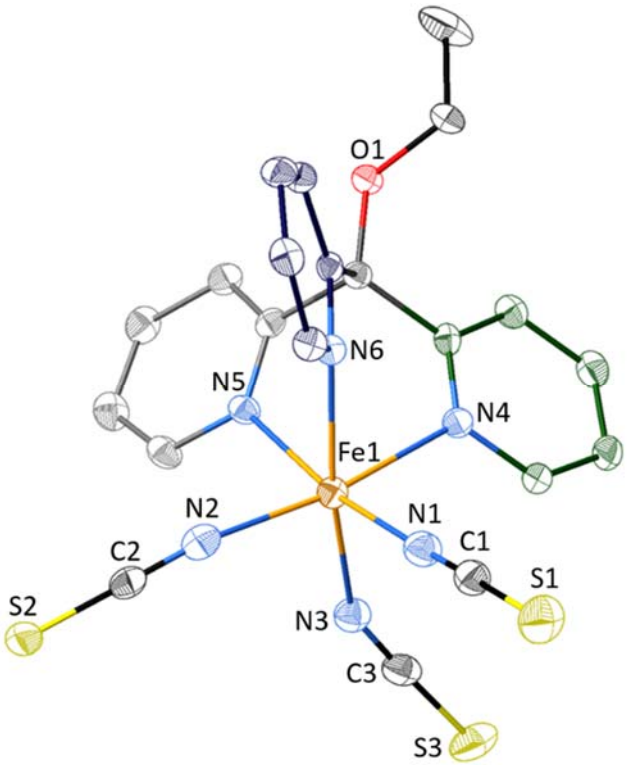

Figure 2. Molecular structure of the anionic complex in **2** showing the Fe(II) environment.

The three N(py)-Fe-N(py) bite angles (chelate angles) of the tripodal ligand are much lower than the corresponding N(NCS)-Fe-N(NCS) angles within the three NCS co-ligands, leading to a strong reduction of ideal symmetry of the pseudo-octahedral FeN_6

coordination spheres. The NCS^- ligands are essentially linear, while the corresponding C-N-Fe angles are significantly bent, as indicated by the angle values 157.5(7)-176.9(6) for **1**, and 153.8(6)-178.2(7) for **2**; the more strongly bent NCS ligands being involved in the shortest intermolecular contacts. Such a distortion of the FeN_6 environment in terms of N-Fe-N angles and Fe-N bond distances is quite usual for such $[Fe(py_3CR)(NCS)_3]^-$ molecular fragments.[55-59,61] As illustrated in Figs S14 and S15, the $[Fe(py_3C\text{-}OEt)(NCS)_3]^-$ anions in **1** and **2** exhibit the same global configuration, in particular for the orientation of the ether groups (C_2H_5O-), with the major difference being in the relative spatial orientations of the three NCS co-ligands.

Table 2. Fe-N bond distances (Å) and the distortion parameters (∑ and *Θ* / °) for **1**-**2**.

Complex	**1**				**2**	
T / K	295		100		150	90
Color	orange		red		yellow	yellow
Fe centre	Fe1A	Fe1B	Fe1A	Fe1B	Fe1	Fe1
Fe1-N1	2.114(6)	2.126(5)	1.940(5)	1.951(5)	2.083(6)	2.089(3)
Fe1-N2	2.107(6)	2.084(5)	1.952(5)	1.960(5)	2.078(7)	2.091(4)
Fe1-N3	2.120(6)	2.102(5)	1.981(6)	1.951(5)	2.086(7)	2.101(4)
Fe1-N4	2.187(5)	2.171(4)	1.939(5)	1.949(5)	2.173(5)	2.180(3)
Fe1-N5	2.267(5)	2.351(4)	1.991(5)	1.986(5)	2.258(5)	2.262(3)
Fe1-N6	2.219(5)	2.188(4)	1.954(5)	1.936(5)	2.156(5)	2.166(3)
<d(Fe-N)>	2.169(6)	2.170(5)	1.959(6)	1.955(5)	2.139(7)	2.148(4)
∑	53.4(2)	56.7(2)	10.6(2)	19.2(2)	54.6(2)	56.4(2)
Θ	107.7(2)	148.7(2)	26.0(2)	68.0(2)	113.6(2)	119.5(2)

Σ is the sum of the deviation from 90° of the 12 *cis*-angles of the FeN_6 octahedron.
Θ is the sum of the deviation from 60° of the 24 trigonal angles of the projection of the FeN_6 octahedron onto its trigonal faces.[70]

The overall crystal packing of **1** consists of interpenetrated anions and cations connected through a network of C-H···S contacts between the sulfur atoms of the NCS^- co-ligands and the carbon atoms of the tripodal py_3C-OEt ligand (see Figs 3a, S16), as well as C-H···S contacts with the carbon atoms of the $[(C_2H_5)_4N]^+$ cations. The shortest hydrogen bonds (C11B···S3A 3.597(5) Å and C17B···S1A$^{(a)}$ 3.522(6) Å) correspond to direct anion···anion contacts, all other CH···S contacts ensuring the cohesion of the

crystal packing in compounds **1** are significantly greater than the sum of the corresponding van der Waals radii (C···N 2.85 Å; C···S 3.50 Å). The connection between adjacent $[Fe(py_3C\text{-}OEt)(NCS)_3]^-$ anions in **1**, lead to supramolecular tetramolecular units (see details below) which are sensitive to the temperature variation. The shortest Fe1···Fe1 intermolecular distances are very similar between the two different anions (Fe1A···Fe1A = 8.4572(19) Å, Fe1B···Fe1B = 8.887(2) Å, Fe1A···Fe1B = 9.8263(16) Å). All together, the fact that the contacts between the spin-active anions are direct and that the intermolecular distances are similar between the two symmetrically independent anions both favour the strong cooperativity in **1**.

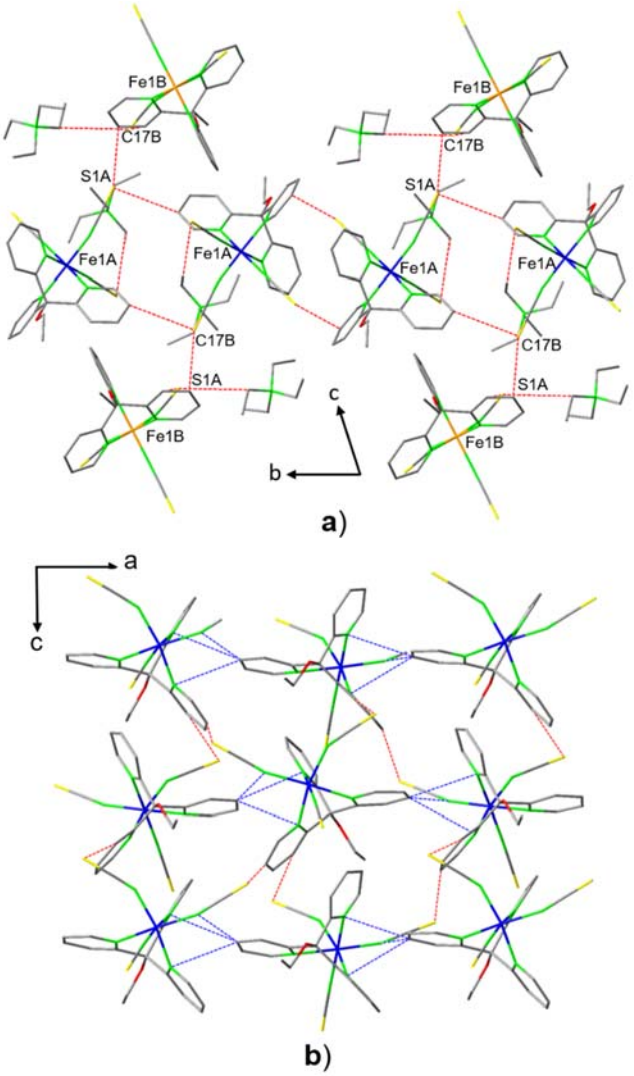

Figure 3. Shortest intermolecular contacts in polymorphs **1** (**a**) and **2** (**b**): C···S and C···N distances in the ranges 3.4-3.7 Å and 3.3-3.5 Å, respectively.

By comparison, the crystal packing of **2** can be pictured as alternated layers of anions and cations, stacked along the crystallographic ***b*** direction (Fig. 3b, Fig. S16).

As for polymorph **1**, the main intermolecular contacts are due to C-H···S contacts between the sulfur atoms of the NCS^- co-ligands and the carbon atoms of the tripodal py_3C-OEt ligand and the carbon atoms of the $[(C_2H_5)_4N]^+$ cations. In addition, weak C-H···N hydrogen bonds between the CH groups (aromatic ring) and nitrogen atoms of adjacent tris-(pyridin-2-yl)ethoxymethane (py_3C-OEt) ligands contribute to the crystal packing. The shortest Fe1···Fe1 distances (Fe1···Fe1 = 8.4440(12) Å, Fe1···Fe1 = 9.8720(14) Å) are in the same range than those characterized for polymorph **1**. As a consequence, there is no structural obvious argument to claim that one polymorph is more cooperative than the other one.

Thermo- and Photomagnetic Properties for 1 and 2. The magnetic studies of **1** and **2** were performed in the temperature range 10-280 K. For both complexes, the thermal variation of the $\chi_m T$ product (χ_m is the molar magnetic susceptibility) is depicted in Fig. 4. The $\chi_m T$ values at 280 K for **1** (≈ 3.664 cm^3 K mol^{-1}) and for **2** (≈ 3.638 cm^3 K mol^{-1}) are almost similar, and close to the values expected for isolated *HS* Fe(II) ions.[54-59,61-64] Upon cooling, the $\chi_m T$ value of **1** remains almost constant down to approximately 150 K where it shows abrupt decrease around 120 K, reaching a value of *ca.* 0.20 cm^3 K mol^{-1}.

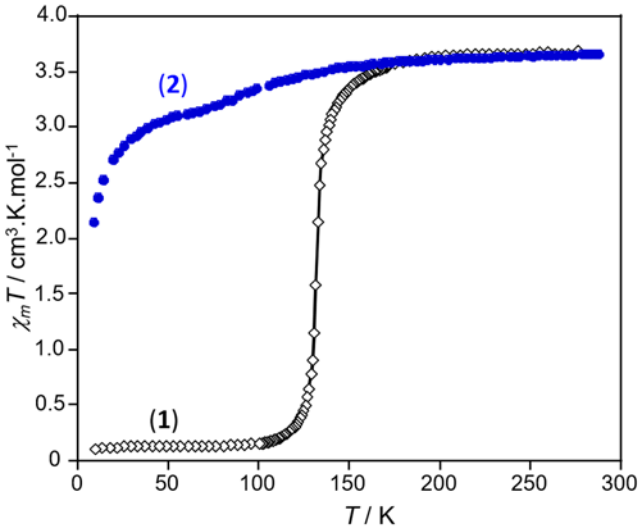

Figure 4. Thermal evolution of the $\chi_m T$ product for polymophs **1** and **2.** The cooling and warming scans overlap almost perfectly.

At lower temperature, the $\chi_m T$ value drops to 0.10 $cm^3 \cdot K \cdot mol^{-1}$ consistent with all Fe^{II} centers in the *LS* state. This behavior indicates the presence of a complete *HS*/*LS* transition at 132.3 K (Fig. 4). As for **1**, upon cooling, the $\chi_m T$ value of **2**, remains constant down to approximately 150 K where a slight gradual decrease occurs to reach a value of *ca.* 3.25 cm^3 K mol^{-1} at 50 K, in agreement with the presence of *ca.* 89 % *HS* for the Fe(II) ions. The decrease observed below 20 K is attributed to the presence of a zero field splitting (ZFS) of the *HS* Fe(II) ions. Finally, the slight gradual decrease of the $\chi_m T$ product observed for compound 2 could be attributed to the presence of *ca.* 5.5 % impurity of **1** in the polycrystalline sample of **2** used for the magnetic characterization. The fact that this $\chi_m T$ decrease occurs slightly below the transition temperature of **1** ($T_{1/2}$ = 132.3 K) does not point any inconsistency with this assumption since it is well known that the *SCO* diluted systems exhibit more gradual transition with lower transition temperature with respect to the pure phases.[71-72] This assumption is further confirmed by two experiments. The first one is the relaxation kinetics recorded at 50 K and 75 K that do not show any time dependence of the $\chi_m T$ value. This clearly indicates that there is no kinetic trapping of any species and that this behavior is not coming from a partial spin crossover of **2** (see Fig. S17). The second experiment is the light-irradiation at 10 K and 510 nm that allows the population of a *HS* metastable state exhibiting a *T(LIESST)* of 68 K (see Fig. S17). This photo-switching involves around 5 % of the material and the *T(LIESST)* relaxation clearly corresponds to the photo-switching behavior of **1** described below (Fig. 5). These two experiments are strongly in favour of the presence of ~ 5 % impurity of polymorph **1** in this sample.

Irradiation of compound **1** at 10 K with green laser light (λ = 510 nm, 6 $mW.cm^{-2}$) resulted in an intense increase of the magnetic signal (Fig. 5). After one hour of irradiation, the light was switched off and the temperature increased at a rate of 0.4 $K.min^{-1}$, corresponding to the standard measurement of the *T(LIESST)* temperature.[68] The comparison between the maximum of the $\chi_m T$ value of the *HS* photo-induced state (3.389 cm^3 K mol^{-1}) and that observed in the dark at high temperature (3.677 cm^3 K mol^{-1}), where the systems is in a 100 % *HS* state, reveals that at low temperature the photo-

conversion reaches almost 100 % of the *HS* state in the bulk material. When the sample was warmed up in the dark, a thermally activated relaxation of the photo-induced *HS* state was reached, leading to a relaxation temperature *T(LIESST)* of 70 K (minimum $\partial\chi_m T/\partial T$ derivative of the $\chi_m T$ *vs. T* plot, Inset Fig. 5).

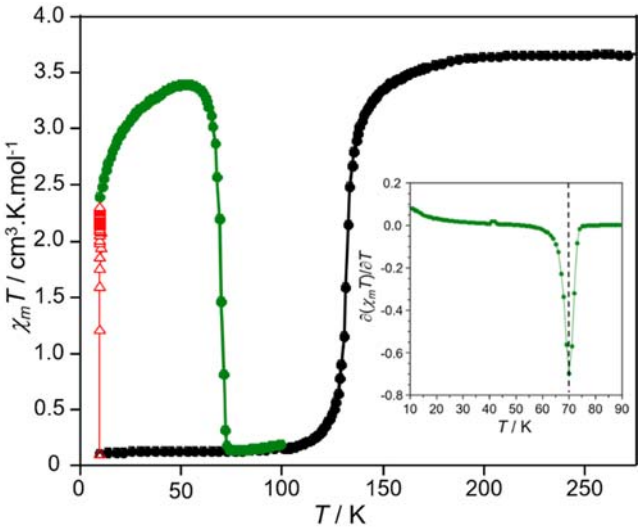

Figure 5. Thermal variation of the $\chi_m T$ product of **1** from 280 to 10 K in the dark (●); under 510 nm light irradiation at 10 K (Δ). Green dots (●) correspond to the subsequent thermal relaxations in the dark. Inset: Plot of $\partial\chi_m T/\partial T$ versus temperature, the minimum indicates the *T(LIESST)* value of 70 K. The temperature sweep rate and the power intensity were 0.4 K.min^{-1} and 6 mW.cm^{-2}, respectively.

Temperature dependent infrared spectroscopy for compounds 1-2. To confirm the conclusion derived from the magnetic data such as the spin sates of the Fe(II) centres at room and low temperatures, the complete *HS* to *LS* transition for **1** and the presence of a small fraction of **1** in the polycrystalline sample of complex **2**, we have recorded infrared spectra in the range corresponding to the stretching vibration ($\nu_{C\equiv N}$) of the NCS groups (2025-2150 cm^{-1}) since the intensities of such vibrations are very sensitive to the spin state of the complex.[59,73-80] For both complexes, the infrared spectra have been recorded using regular KBr pellets which impose the crushing of single crystals.

For **1**, according to the thermal dependences of the $\chi_m T$ product and to the thermal evolution of the metastable *HS* state depicted in Fig. 5, we have recorded the infrared spectra at 200 and 10 K, at 10 K under irradiation and at 80 K after relaxation from the

photo-induced *HS* to the *LS* states. The resulting infrared spectra in the region of the NCS stretching vibrations (2025-2150 cm^{-1}) are depicted in Fig. 6a.

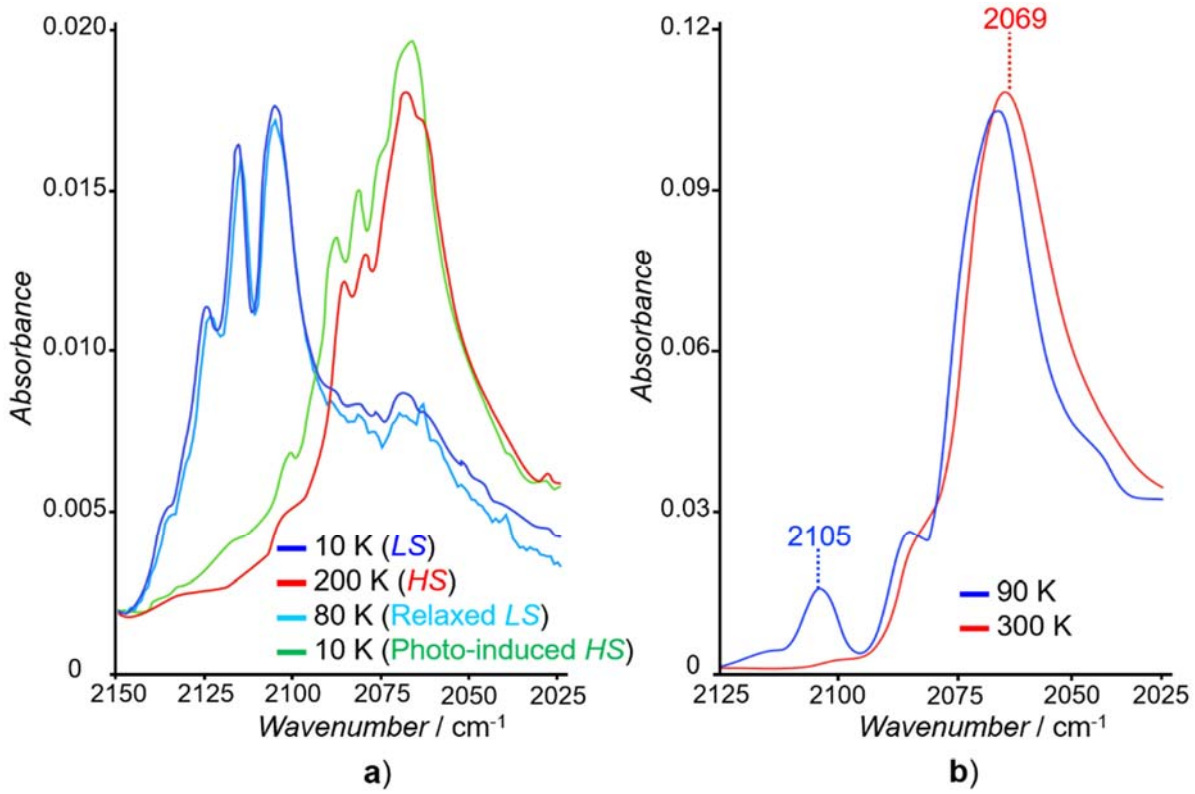

Figure 6. **a**) Principal infrared bands in the range 2025-2150 cm^{-1} spectra for compound **1**: at 200 K (—) for high temperature *HS* state, 10 K (—) for the *LS* sate, 10 K under light irradiation for the *HS* photo-induced *HS* state (—) and at 80 K for the relaxed *LS* sate (—), see Fig. S18 for the wavenumber for each band; **b**) Infrared spectra for compound **2** in the 2025-2125 cm^{-1} region at 90 and 300 K.

The infrared spectrum performed at 200 K (see red bands in Fig. 6a) displays three strong vibration bands around 2080 cm^{-1} (2069, 2080 and 2089 cm^{-1}) which are attributed to the *HS* state (and will be considered as a spectral signature of the *HS* state hereafter), in relation with the full *HS* state derived from the magnetic data above 160 K. The observed splitting of the vibration bands is due to the presence of two symmetry independent $[Fe(py_3C\text{-}OEt)(NCS)_3]^-$ anions and to their low symmetry in the *P-1* space group, leading to coupling in the NCS stretching modes. At 10 K, that is below the thermal *HS* to *LS* transition revealed by the magnetic results, the infrared spectrum shows that the characteristic bands of the NCS stretching vibrations are shifted to higher frequencies (2105, 2116 and 2125 cm^{-1}). This is expected owing to higher force constants in the *LS* state (typical frequency shift of nearly 40 cm^{-1}). Under

irradiation at 10 K (λ = 505 nm, 40 mW, 5 min), the resulting spectrum (see green bands in Fig. 6a) displays vibration bands (2067, 2079, and 2087 cm^{-1}) almost similar to the 200 K *HS* state, confirming the full *LS* to *HS* conversion under irradiation, as revealed by the photo-magnetic data (Fig. 5). Starting from the photo-induced *HS* state, the temperature was further increased to 80 K; the resulting infrared spectrum appears very similar to the previously measured 10 K *LS* state, confirming the complete *HS* to *LS* relaxation. At last, the two spectra characteristic of the *HS* states at 200 and 10 K (red and green bands in Fig. 6a), in particular the spectrum recorded at 10 K under irradiation, show weak broad bands at higher frequency, around the characteristic region of the *LS* state, as well as the two spectra attributed to the *LS* state (blue and aqua bands in Fig. 6a) which display relatively weak bands at lower frequency around the *HS* region. These weak and broad bands could be attributed to the presence of very low fraction of the corresponding spin state, and therefore should not question the complete thermal *SCO* transition and the full *HS* to *LS* conversion under irradiation, discussed above for compound **1**. For **2**, according to the magnetic data shown in Fig. 4, the infrared spectra have been recorded only at 300 and 90 K (Fig. 6b). The room temperature spectrum confirms the presence of a full *HS* sate as revealed by the magnetic studies. At low temperature (90 K), although this *HS* spin band remains virtually unchanged (marginally shifted to slightly higher frequencies owing to 300K-90K thermal effects), a second band of moderate intensity appears at higher frequency in the characteristic region of the *LS* state. This latter is indeed located at a similar frequency than the corresponding value observed for the strongest band observed for **1** in the *LS* region (2105 cm^{-1}). This observation supports further the presence of a low fraction of **1** in the polycrystalline sample of polymorph **2**, as revealed by the magnetic data.

Magneto-Spectroscopic and Structural relationships for compounds 1-2. Following the conclusions derived from the infrared spectra on *HS* and *LS* states of both thermal and photo-induced transitions in compound **1** (see Fig. 6a), we have

recorded the infrared spectra with temperature, in the region corresponding to the NCS stretching vibration for this compound. According to the magnetic behavior (see Fig. 5), the infrared spectra were recorded in the 200-10 K range for the thermo-magnetic transition (Fig. 7a) and in the range 10-80 K for the photo-magnetic behavior, including the *HS* to *LS* relaxation (Fig. 7b).

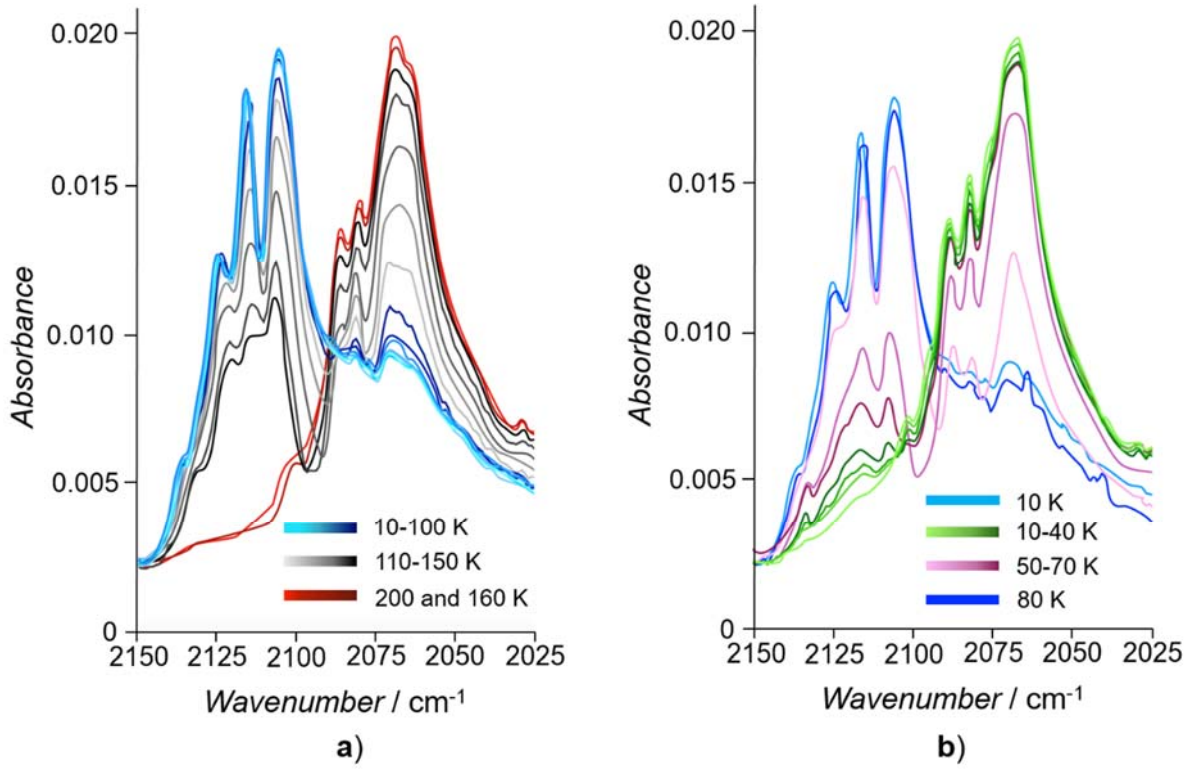

Figure 7. (**a**) Temperature dependences (cooling mode), in the dark, of the infrared spectra from 200 to 10 K; (**b**) infrared spectra at 10 K (—) in the dark, at 10K (—) after irradiation (λ = 505 nm, 40 Mw, 5 mn) and while raising the temperature from 10 K to 80K in the dark (**b**), for the crushed single crystals of **1**.

As clearly depicted in Fig. 7a, the intensities of the three $\nu_{C\equiv N}$ vibrational bands (2069, 2080 and 2089 cm^{-1}), signature of the *HS* state, do not show any modification upon cooling to 160 K. From 150 K to 110 K, these bands decrease in intensity, and do not show any strong dependence upon further cooling from 110 K to 10 K. In addition, from 150 K to 110 K, the vibration bands at higher energies (2105, 2116 and 2125 cm^{-1}), signature of the *LS* state appear and gradually increase with decreasing the temperature. The three $\nu_{C\equiv N}$ bands characteristic of the metastable *HS* state, change similarly when the temperature was increased in the dark from the photo-induced *HS*

state at 10 K (2067, 2079 and 2087 cm^{-1}) to the relaxed *LS* at 80 K (2105, 2116 and 2125 cm^{-1}) (see Fig. 7b): the intensities of the three $\nu_{C\equiv N}$ bands (2067, 2079 and 2087 cm^{-1}), assigned to the *HS* state, first stay constant from 10 K to 40 K, and then abruptly decrease in intensity from 50 K to 60 K. In parallel, three other bands, attributed to the *LS* state, appear at higher frequencies (2105, 2116 and 2125 cm^{-1}) whose intensities increase with increasing the temperature. This behavior is perfectly consistent with the conclusions drawn from the thermo-magnetic and photo-magnetic investigations.

The Fe-N bond lengths (<d(Fe-N)>) and distortion parameters (∑ and Θ) summarized in Table 2 for the polymorph complexes **1** and **2** confirms the presence of almost full *HS* state for **1** at 295 K and for **2** at 150 K, in agreement with the magnetic data (Fig. 3) and with the infrared spectroscopy (Fig. 6). As discussed above, the slight gradual decrease of the $\chi_m T$ product observed for compound **2** has been attributed to the presence of *ca.* 5.5 % impurity of **1** in the polycrystalline sample of **2** used for the magnetic characterization. However, this analysis is not the only one since the decrease could also be at the origin of a presence of a gradual and incomplete *SCO* transition in complex **2**. In order to remove any doubt about this assumption, we have determined the single crystal structure of **2** at 90 K (see Tables 1-2), which clearly reveals almost similar Fe-N distances and distortion parameters (<d(Fe-N)> = 2.148(4) Å; ∑ = 56.4(2); Θ = 119.5(2)°) than those observed at 150 K for the full *HS* state (<d(Fe-N)> = 2.139(7) Å; ∑ = 54.6(2)°; Θ = 113.6(2)°). For **1**, the crystal structure at 100 K shows a significant contraction of the FeN_6 octahedron and lower angular distortion parameters (∑ and Θ) with respect to the room temperature data (<d(Fe-N)>/∑ / Θ for Fe1A and Fe1B centres are respectively: 2.169(6) Å / 53.4(2)° / 107.7(2)° and 2.170(5) Å / 56.7(2)° / 148.7(2)° at 295 K; 1.959(6) Å / 10.6(2)° / 26.0(2)° and 1.955(5) Å / 19.2(2)° / 68.0(2)° at 100 K). The characterized shortening of the Fe-N bond distances is in agreement with the *LS* state, synonym of the presence of a *SCO* transition as revealed by the magnetic data (see Fig. 3) and by the infrared results (see Fig. 6a). In addition, the dispersion in Fe-N bond distances is much reduced at 100 K, while the two distortion parameters (∑ and Θ) drastically decreases. These two effects result from the enhancement of the covalency

of the Fe-N bonds in the *LS* state with the *sp* hybridized N1, N2, N3 atoms and sp^2 hybridized N4, N5, and N6 atoms for the two anions. The values of the Fe-N distance, and trigonal distortion are in the range of the values reported for similar $[Fe(py_3CR)(NCS)_3]^-$ anions undergoing SCO.[55-59,61] For polymorph **2**, no similar thermal evolution is observed (see Table 2), in agreement with the absence of any SCO for **2**. As expected, this *SCO* transition of **1**, associated to a *HS-LS* molecular volume contraction, affects the unit cell parameters accordingly (see Table 1). In order to shed light on the effect of the *SCO* transition on the structural parameters, including the crystal packing in **1**, we have studied the thermal evolution of the unit cell parameters in the vicinity of the transition temperature (200-95 K). The resulting behavior, summarized in Fig. 8, shows that the *a*, *b* and *c* parameters, as well as the unit cell volume display significant anisotropic changes at the transition temperature ($T_{1/2}$ = 132.3 K). Indeed, upon cooling, in the high temperature region (200-140 K), all the parameters (*a, b, c* and *V*) show gradual decrease which is attributed essentially to the expected thermal contraction in the *HS* state, but in the vicinity of the transition temperature, an expansion occurs in the *ab* plane (simultaneously for the *a* and *b* parameters), and paralleled, more strongly, by a contraction of the *c* parameter.

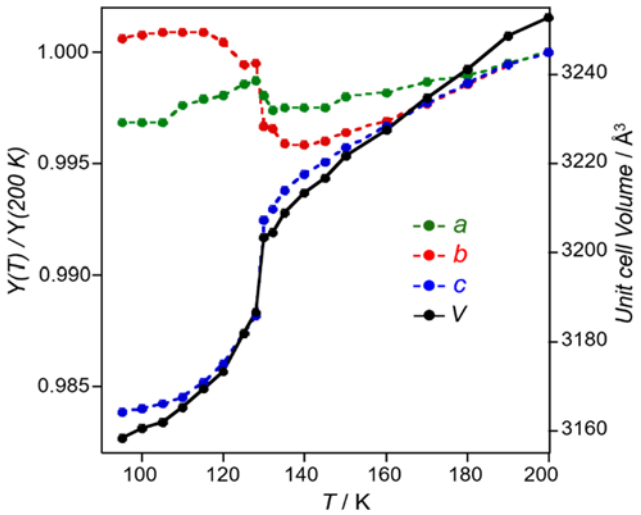

Figure 8. Thermal dependence of the lattice parameters for **1** in the temperature range 95-200 K, showing the anisotropic changes in the vicinity of *HS* to *LS* transition. *Y(T)/Y(200 K)* corresponds to the relative value of each cell parameter (*a*, *b* and *c*).

As described above for **1**, the two more significant intermolecular contacts C-H···S hydrogen bonds observed at room temperature (295 K) between two adjacent $[Fe(py_3C\text{-}OEt)(NCS)_3]^-$ anionic complexes (C11B···S3A 3.597(5) Å and C17B···S1A$^{(a)}$ 3.522(6) Å), lead to supramolecular tetranuclear units depicted in Fig. 9. However, at low temperature (100 K), in the *LS* region, the C17B···S1A$^{(a)}$ contact remains almost unchanged (3.522(6) Å and 3.482(6) Å at 295 and 100 K, respectively), while the C11B···S3A contact (3.597(5) and 3.475(5) Å at 295 and 100 K, respectively) shows a more significant effect to the *SCO* transition, which results in a contraction of the tetranuclear units as also revealed by significant shortening of the two Fe···Fe distances, defining each tetranuclear unit, by *ca.* 0.5 Å (Fe1A···Fe1B 9.826(1) Å at 295 K and 9.286(1) Å at 100 K; Fe1A…Fe1B$^{(a)}$ 12.450(1) Å at 295 K and 11.979(1) Å at 100 K). According to the crystallographic directions of these Fe···Fe distances (Fe1A···Fe1B roughly along the [001] direction, and Fe1A…Fe1B$^{(a)}$ roughly along the [11-1] direction), the large shortenings occurring upon cooling from 295 to 100 K resulted essentially from the *SCO* transition, since the thermal evolution of the cell parameter revealed clearly that the main structural changes accompanying the *SCO* transition occur essentially along the [001] direction.

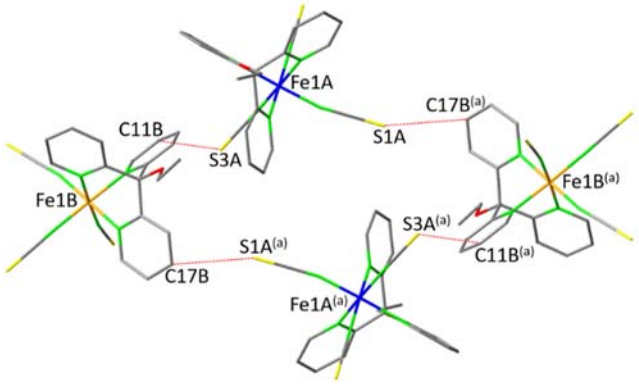

Figure 9. The most significant intermolecular contacts in polymorph **1:** C11B···S3A: 3.597(5) Å at 295 K, 3.475(5) Å at 100 K; C17B···S1A$^{(a)}$: 3.522(6) Å at 295 K, 3.482(6) Å at 100 K. Codes of equivalent position: (a) 1-x,1-y,-z.

One important question is raised from the different thermo-magnetic behavior of the two polymorphs. Indeed, only compound **1** exhibits a thermal SCO. To our knowledge, compound **2** is the only similar $[Fe(py_3CR)(NCS)_3]^-$ anion which does not

undergo SCO.[55-59,61] It is well accepted that the spin crossover phenomenon results from a subtle energetic balance between electron paring energy, ligand field effects, and intermolecular couplings through hydrogen bonds, π-π stacking, or weak Van der Waals interactions. As discussed in the previous section, the comparative analysis of the crystal packing of compounds **1** and **2** does not show any direct evidence for a difference in cooperativity. In particular, compound **2** is not involved in specific intermolecular contacts, which could block any potential spin crossover. A close comparison of the molecular structural parameters may be used to interpret this fact. In our previous investigation of the SCO properties of the $[Fe(py_3C\text{-}OEt)_2][Fe(py_3C\text{-}OEt)(NCE)_3]_2.2CH_3CN$ compounds (E = S and BH_3), we have found that the lower $T_{1/2}$ SCO thermal transition, and correlatively stabilisation of the *HS* state, for the thiocyanate compound by comparison with the cyanotrihydroborate one is directly related to a bent geometry of the Fe-NC(S) groups (see Table S1), which in turn promotes a weaker ligand field on the Fe(II) ion.[59,63-64] The same explanation holds here for compound **2**. Although the Fe-N bond distances and Σ and Θ angular distortion parameters do not exhibit an obvious trend, the three Fe-NC(S) angles characterized for the 150 K crystal structure (178.2(7)°, 164.0(6)°, and 153.8(6)°) present specific features. Especially Fe-N3-C3(S3) angle deviates strongly from linearity, and is furthermore the lowest value observed for the complete $[Fe(py_3CR)(NCS)_3]^-$ series of compounds published to date.[55-59,61] We may therefore conclude that the ligand field at the Fe(II) site in compound **2** is too weak to provoke a thermal spin transition, as observed previously for the *HS* dinuclear complex $[\{Fe(tpc\text{-}Obn)(NCS)(\mu\text{-}NCS)\}_2]$ based on similar tripodal ligand, for which the κN-bound terminal NCS co-ligand displays a low Fe-N-C angle (156.6(4)°) almost as far from the linearity.

Discussions. To further explore these thermal dependences of the properties of polymorph **1**, we have plotted the thermal evolution of the maximum absorbance for $\nu_{C\equiv N}$ vibrational band located at 2069 cm^{-1} in the temperature range 200-10 K, and for the $\nu_{C\equiv N}$ vibrational band located at 2105 cm^{-1} recorded in the dark (after irradiation at

10K), in the temperature range 10-80 K (Fig. 10). As expected, this plot shows a clear regime change around 130 K, corresponding to the *SCO* transition region, and abrupt increase of the relative absorbance at 10 K after light irradiation, that remains constant in the dark before a gradual decrease in the temperature range 50-80 K, recalling the thermal evolution of the metastable *HS* state in the dark and the relaxation behavior revealed by the magnetic data. This was confirmed by plotting $\partial(abs)/\partial T$ as a function of temperature indicating a minimum value of 70 K, corresponding to the value of the *T(LIESST)* derived from the magnetic data (see Inset Fig. 10). Last but not least, similar behaviors are observed when the thermal evolution of the maximum of the relative absorbance of the four other vibrational bands (2125, 2116, 2105 and 2069 cm^{-1}) are examined, as clearly depicted in Fig. S19.

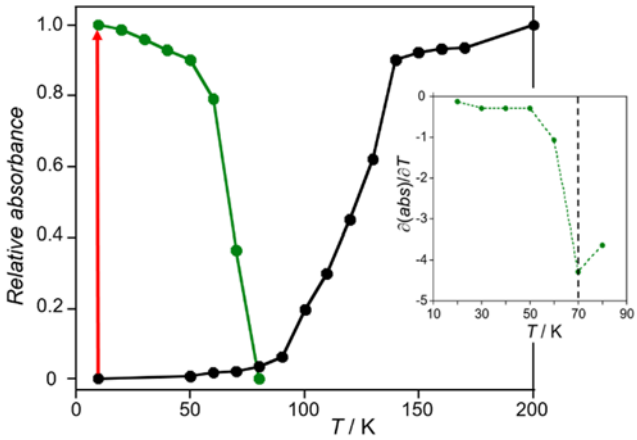

Figure 10. Temperature dependences of the the relative absorbance of the $\nu_{C\equiv N(HS)}$ (ABS *vs*. *T*) vibration band observed at 2069 cm^{-1} from 200 to 10 K in the dark (●); temperature dependences of the relative absorbance of the $\nu_{C\equiv N(LS)}$ (1-ABS *vs*. *T*) band observed at 2105 cm^{-1} under 505 nm (—), with a power intensity of 40 mW, light irradiation at 10 K, for the crushed single crystals of **1**. Green dots (●) are the subsequent thermal relaxation in the dark. Inset: Plot of $\partial(abs)/\partial T$ versus temperature indicating *T(LIESST)* value of 70 K.

The overall consistency of the infrared data has been established by correlating the thermal dependence of the $\chi_m T$ product including the *LIESST* effect and the thermal variation of the relative absorbance of the infrared bands discussed above (see Fig. 7). The resulting behaviors summarized in Fig. 11, show an excellent correlation between the thermal evolution of the $\chi_m T$ product and the relative absorbance of the two vibrational bands observed at 2069 and 2105 cm^{-1}, which clearly show significant

changes in the temperature regions where the thermal and the photo-induced spin transitions occur. The more gradual trend observed for the decrease of the relative absorbance of the $\nu_{C\equiv N}$ band should arise from the sample preparation of **1** for the infrared study: the crushed single crystals in the KBr pellets exhibit different sizes,

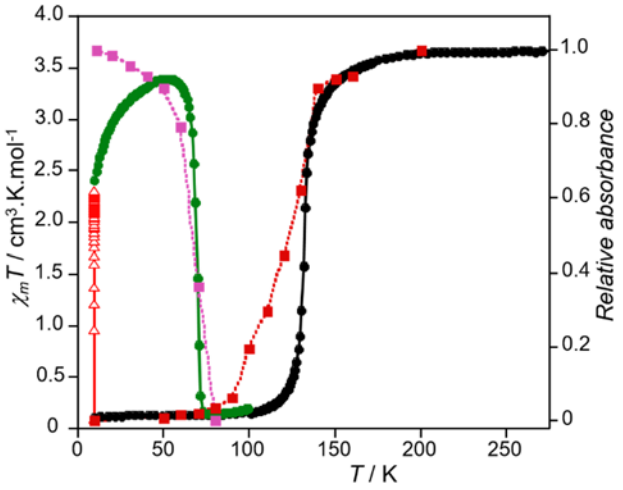

Figure 11. Temperature dependences of the $\chi_m T$ product (●) including the metastable photo-induce *HS* state (●) and of the relative absorbance of the $\nu_{C\equiv N(HS)}$ (ABS *vs*. *T*) bands observed at 2069 cm^{-1} (■) and the $\nu_{C\equiv N(LS)}$ (1-ABS *vs*. *T*) at 2105 cm^{-1} (■) at 10 K after light irradiation, for the crushed single crystals of **1**.

shapes and orientations, as previously observed in similar KBr pellets and thin films of [Fe(H$_2$Bpz)$_2$(phen)] and [Fe(H$_2$Bpz)$_2$(bipy)] (H$_2$Bpz = bis(pyrazolyl)borate), bipy = 2,2'-bipyridine, 1,10-phenanthroline).[81] Optical microscopy investigations conducted on a large set of randomly oriented single crystals of [{Fe(NCSe)(py)$_2$}$_2$(m-bpypz)] (m-bpypz = 3,5-bis(2-pyridyl)-pyrazolate) taken from the same batch revealed that the transition temperature is strongly affected by the size and the shape of the single crystals.[82] Thus the gradual thermal behavior (see red points in Fig. 11) results probably from the presence of several small single crystals of different sizes and shapes in the KBr pellet. The significant divergence of the relative absorbance with respect to the magnetic data around 10 K could be attributed to the ZFS effect which contributes to significant decrease of the magnetic signal.

In order to confirm the origin of the gradual evolution of the relative absorbance of the $\nu_{C\equiv N}$ bands (see Fig. 11) of **1**, we have elaborated a uncommon protocol allowing

the use of a single crystal sample, consisting of careful painting a tiny layer of nujol oil on a KBr pellet on which single crystals are sprinkled. IR spectra were then recorded from 90 to 220 K upon the thermal spin transition (see Fig. 12).

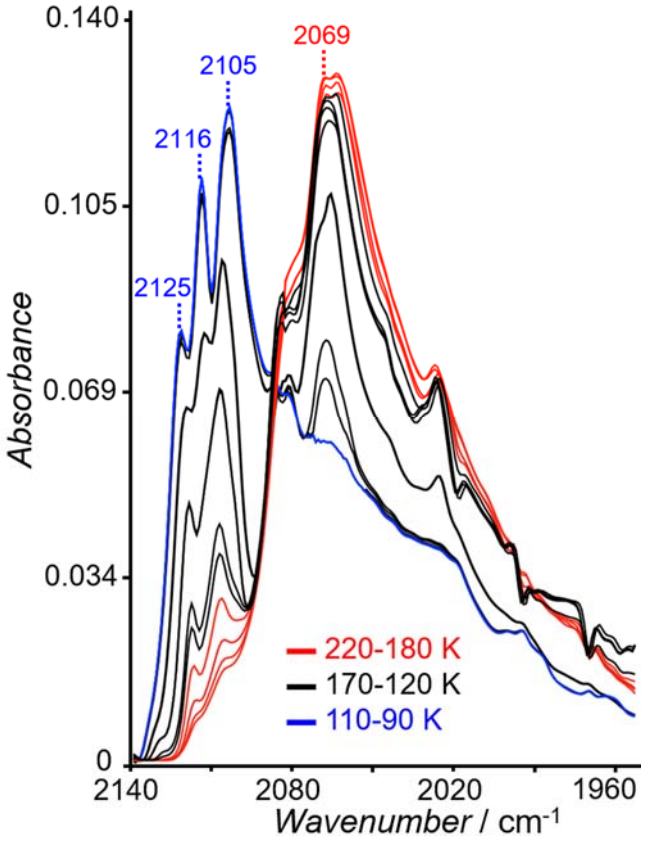

Figure 12. Temperature dependences of the infrared spectra (1950-2140 cm^{-1}) in the temperature region 220-90K for single crystals sample of compound **1**.

As for the crushed sample, we have correlated the thermal dependence of the relative infrared absorbance of the selected vibrational bands (2069, 2105, 2116 and 2125 cm^{-1}) depicted in Fig. 12 with the thermal evolution of the $\chi_m T$ product. The resulting behaviors (Fig. 13) show an excellent correlation between the two thermal dependences, supporting the fact that the polycrystalline powder resulting from the crushed single crystals of **1** is at the origin of the gradual behavior depicted in Fig. 11.[81-82]

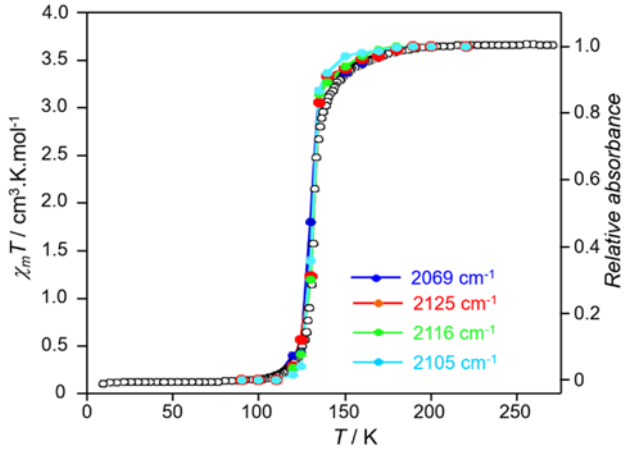

Figure 13. The thermal $\chi_m T$ product (o) and the relative absorbance of the four principal ν(CN) bands observed for single crystals sample of compound **1**. ABS *vs*. *T* for the IR band assigned for the *HS* state ($\nu_{C\equiv N}$ = 2069 cm^{-1}), (1-ABS) *vs. T* for the IR bands assigned for the *LS* state ($\nu_{C\equiv N}$ = 2105, 2116, 2125 cm^{-1}).

■ CONCLUSIONS

In summary, this work describes a pair of Fe(II) polymorphs, $[(C_2H_5)_4N]_2[Fe(py_3C\text{-}OEt)(NCS)_3]_2$ (**1**) and $[(C_2H_5)_4N][Fe(py_3C\text{-}OEt)(NCS)_3]$ (**2**), as the first anionic polymorphs for which one of them exhibits SCO behavior. The two complexes have been prepared as polycrystalline powders and as single crystals using established appropriate protocols that clearly discriminate the nucleation and the crystal growth of each complex. Both have been structurally characterized and their thermo- and photo-induced spin state changes were correctly tracked using detailed magnetic and infrared spectroscopy investigations. In both complexes, the molecular structure is composed by the same anionic $[Fe(py_3C\text{-}OEt)(NCS)_3]^-$ complex (two units for **1**, and one unit for **2**) involving a metal centre, one py_3C-OEt tridentate ligand and three terminal κN-SCN terminal co-ligands. Polymorph **2** exhibits a *HS* state in the whole temperature range studied (300-10 K), while for complex **1**, the thermal variation of the $\chi_m T$ product shows an almost abrupt and complete *SCO* transition centred at *ca.* 132.3 K. X-ray diffraction studies at low temperature (100 K) show a strong modification of the iron (II) coordination sphere, in agreement with the presence of a SCO transition in **1**. This was further supported by the thermal evolution of the unit cell of **1**, which also revealed the anisotropic character of the *SCO* transition.

Irradiation of **1** at 10 K revealed a gradual increase of the magnetic moment that vanishes as the temperature is increased with an inflexion point at *ca.* 70 K, corresponding to the *T(LIESST)* value. Last but not least, the thermal dependence of the infrared spectroscopy indicated, through the thermal evolution of the maximum absorbance for ν(NCS) vibrational bands in the temperature range 200-10K, and in the range 10-80 K in the dark (after irradiation at 10K), *(i)* a clear regime change around 130 K, corresponding to the *SCO* transition region derived from the magnetic and structural studies; *(ii)* abrupt changes of the relative absorbance at 10K after light irradiation, that remains constant in the dark; *(iii)* followed by a gradual change in the temperature range 50-80 K. The plot of $\partial(abs)/\partial T$ as a function of temperature shows a minimum value of 70 K, in good agreement with the value of the *T(LIESST)* value derived from the magnetic data. The origin of the absence of spin crossover for compound **2** has been attributed to a more constrained geometry with bent Fe-NC(S) groups, decreasing the generated ligand field at the Fe(II) site.[63] The more bent geometry originates from specific intermolecular contacts. The difference in SCO behavior between the two polymorphs shows the possibility to tune the properties in this new family of anionic Fe(II) complexes by controlling the crystal packing. Finally, the inconsistency observed, for **1**, between the abrupt *SCO* derived from the magnetic data and the gradual behavior extracted from the infrared spectra, led us to the use of a non-regular experimental protocol to record the infrared spectra. The latter is based on the use of a single crystal sample in place of polycrystalline powder resulting from the crushing of single crystals induced during the preparation of the KBr pellets. This leads to abrupt evolution of the relative absorbance of the $\nu_{C\equiv N}$ bands of **1** which fits perfectly with the abrupt thermal behavior derived from the magnetic data. In the synthetic point of view, it is important to mention that the two polymorphs are prepared as tetraethylammonium salts which are stable and soluble in organic solvents. This allows the possibility to perform easily several metatheses to introduce functional cations such as SCO cationic complexes, fluorescent cations or electron-

donor molecules such tetrathiafulvalene (TTF) derivatives for the design of multifunctional systems, such as fluorescent or conducting switchable materials.[6,60]

■ ASSOCIATED CONTENT

Supporting information

The Supporting Information is available free of charge on the ACS Publications website at DOI: XXXXX/acs.inorg-chem.XXXXXXX

X-ray crystallographic data in CIF format: CCDC numbers 2025933-2025936 (CIF).
This material is available free of charge via the Internet at http://pubs.acs.org.
Syntheses details and figures S1-S19 (pdf)

■ AUTHOR INFORMATION

Corresponding author

Smail Triki — *Univ Brest, CNRS, CEMCA, 6 Avenue Le Gorgeu, C.S. 93837 - 29238 Brest Cedex 3, France; orcid.org/0000-0003-0130-7461; E-mail: smail.triki@univ-brest.fr*

Authors

Emmelyne Cuza — *Univ Brest, CNRS, CEMCA, 6 Avenue Le Gorgeu, C.S. 93837 - 29238 Brest Cedex 3, France;*

Cle Donacier Mekuimemba — *Univ Brest, CNRS, CEMCA, 6 Avenue Le Gorgeu, C.S. 93837 - 29238 Brest Cedex 3, France;*

Nathalie Cosquer — *Univ Brest, CNRS, CEMCA, 6 Avenue Le Gorgeu, C.S. 93837 - 29238 Brest Cedex 3, France;* orcid.org/0000-0002-2752-3130

Françoise Conan — *Univ Brest, CNRS, CEMCA, 6 Avenue Le Gorgeu, C.S. 93837 - 29238 Brest Cedex 3, France; orcid.org/0000-0002-0954-259X*

Sébastien Pillet — *Laboratoire de Cristallographie, Résonance Magnétique et Modélisations, UMR 7036, Boulevard des aiguillettes, BP239 54506 Vandoeuvre-les-Nancy, France;* orcid.org/0000-0002-5441-6322

Guillaume Chastanet — *CNRS, Université Bordeaux, ICMCB, 87 Av. Doc. A. Schweitzer, F-33608 Pessac, France; orcid.org/0000-0001-6829-4066*

Author Contributions

The manuscript was written through contributions of all authors. All authors have given approval to the final version of the manuscript.

Notes

The authors declare no competing financial interest.

■ ACKNOWLEDGMENTS

The authors acknowledge the CNRS (Centre National de la Recherche Scientifique), the "Université de Brest". EC thanks the financial support from “Région de Bretagne (AReD) and Université de Brest (CDE)”. The University of Bordeaux and Région Nouvelle Aquitaine are also acknowledged.

■ REFERENCES

(1) Bartual-Murgui, C.; Akou, A.; Thibault, C.; Molnar, G.; Vieu, C.; Salmon, L.; Bousseksou, A. Spin-crossover metal–organic frameworks: promising materials for designing gas sensors. *J. Mater. Chem. C*, **2015**, *3*, 1277–1285.

(2) Lapresta-Fernandez, A.; Titos-Padilla, S.; Herrera, J. M.; Salinas-Castillo, A.; Colacio, E.; Capitan-Vallvey, L. F. Photographing the synergy between magnetic and colour properties in spin crossover material [Fe (NH_2trz)$_3$](BF_4)$_2$: a temperature sensor perspective. *Chem. Commun.* **2013**, *49*, 288–290.

(3) Linares, J.; Codjovi, E.; Garcia, Y. Pressure and temperature spin crossover sensors with optical detection. *Sensors* **2012**, 12, 4479–4492.

(4) Cuéllar, M. P.; Lapresta-Fernández, A.; Herrera, J. M.; Salinas-Castillo, A.; Pegalajar, M. del C.; Titos-Padilla, S.; Colacio, E.; Capitán-Vallvey, L. F. Thermochromic sensor design based on Fe (II) spin crossover/polymers hybrid materials and artificial neural networks as a tool in modelling. *Sensors and Actuators B*, **2015**, *208*, 180–187.

(5) Rodriguez-Jimenez, S.; Feltham, H. L. C.; Brooker, S. Non-Porous Iron(II)-Based Sensor: Crystallographic Insights into a Cycle of Colorful Guest-Induced Topotactic Transformations. *Angew. Chem. Int. Ed.* **2016**,55, 15067–15071.

(6) Benaicha, B.; Van Do, K.; Yangui, A.; Pittala, N.; Lusson, A.; Sy, M.; Bouchez, G.; Fourati, H.; Gómez-García, C. J.; Triki, S.; Boukheddaden, K. Interplay between Spin-Crossover and Luminescence in a Multifunctional Single Crystal Iron (II) complex: Towards a New Generation of Molecular Sensors. *Chem. Sci.* **2019**, *10*, 6791-6798.

(7) Matsuda, M.; Isozaki, H.; Tajima, H. Reproducible on-off switching of the light emission from the electroluminescent device containing a spin crossover complex. *Thin Solid Films* **2008**, *517*, 1465-1467.

(8) Cobo, S.; Molnár, G.; Real, J.-A.; Bousseksou, A. Multilayer Sequential Assembly of Thin Films That Display Room-Temperature Spin Crossover with Hysteresis. *Angew. Chem. Int. Ed.* **2006**, *45*, 5786 –5789.

(9) Kahn, O.; Martinez, C. J. Spin-transition polymers: from molecular materials toward memory devices. *Science* **1998**, 279, 44–48.

(10) Garcia, Y.; van Koningsbruggen, P. J.; Codjovi, E.; Lapouyade, R.; Kahn, O.; Rabardel, L. Non-classical FeII spin-crossover behaviour leading to an unprecedented extremely large apparent thermal hysteresis of 270 K: application for displays. *J. Mater. Chem.* **1997**, *7*, 857–858.

(11) Murray, K.S.; Kepert, C.J. Cooperativity in Spin Crossover Systems: Memory, Magnetism and Microporosity. *Top. Curr. Chem.* **2004**, *233*, 195-228.

(12) Létard, J.-F.; Guionneau, P.; Goux-Capes, L. Towards Spin Crossover Applications.*Top. Curr. Chem.* **2004**, *235*, 221–249.

(13) Bousseksou, A.; Molnar, G.; Salmon, L.; Nicolazzi, W. Molecular spin crossover phenomenon: recent achievements and prospects. *Chem. Soc. Rev.* **2011**, *40*, 3313-3335.

(14) Rueckes, T.; Kim, K.; Joselevich, E.; Tseng, G. Y.; Cheung, C.-L.; Lieber, C. M. Carbon Nanotube-Based Nonvolatile Random Access Memory for Molecular Computing. *Science* **2000**, *289*, 94-97.
(15) Galet, A.; Gaspar, A. B.; Carmen Muñoz, M.; Bukin, G. V.; Levchenko, G.; Real, J.-A. Tunable Bistability in a Three-Dimensional Spin-Crossover Sensory- and Memory-Functional Material. *Adv. Mater.* **2005**, *17*, 2949–2953.
(16) Guionneau, P.; Marchivie, M.; Bravic, G.; Létard, J.-F.; Chasseau, D. Co(II) molecular complexes as a reference for the spin crossover in Fe(II) analogues. *J. Mater. Chem.* **2002**, *12*, 2546-2551.
(17) Gaspar, A. B.; Carmen Muñoz, M.; Niel, V.; Real, J.-A. $[Co^{II}(4\text{-terpyridone})_2]X_2$: A Novel Cobalt(II) Spin Crossover System [4-Terpyridone = 2,6-Bis(2-pyridyl)-4(1*H*)-pyridone]. *Inorg. Chem.* **2001**, *40*, 1, 9–10.
(18) Zarembowitch, J.; Kahn, O. Magnetic Properties of Some Spin-Crossover, High-Spin, and Low-Spin Cobalt(II) Complexes with Schiff Bases Derived from 3-Formylsalicylic Acid. *Inorg. Chem.* **1984**, *23*, 589-593.
(19) Fürmeyer, F.; Münzberg, D.; Carrella, L. M.; Rentschler, E. First Cobalt(II) Spin Crossover Compound with N4S2-Donorset. *Molecules* **2020**, *25*, 855.
(20) Nik Ibrahim, N. M. J.; Mohd Said, S.; Mainal, A.; Mohd Sabri, M. F.; Abdullah, N.; Megat Hasnan, M. M. I.; Che Hassan, H.; Mohd Salleh, M. F.; Wan Mohd Mahiyiddin, W.A. Molecular design strategies for spin-crossover (SCO) metal complexes (Fe(II) and Co(II)) for thermoelectricity. *Materials Research Bulletin* **2020**, *126*, 110828.
(21) Villaman, D.; McMonagle, C. J.; Probert, M. R.; Peña, O.; Moreno, Y.; Fuentealba, M. Structural studies of a manganese(III) complex with spin-crossover and thermochromic properties. *CrystEngComm* **2020**, *22*, 3221-3233.
(22) Morgan, G. G.; Murnaghan, K. D.; Müller-Bunz, H.; McKee, V.; Harding, C. J. A Manganese(III) Complex That Exhibits Spin Crossover Triggered by Geometric Tuning. *Angew. Chem. Int. Ed.* **2006**, *45*, 7192–7195.
(23) Fitzpatrick, A. J.; Trzop, E.; Müller-Bunz, H.; Dîrtu, M. M.; Garcia, Y.; Collet, E.; Morgan, G. G. Electronic *vs.* structural ordering in a manganese(III) spin crossover complex. *Chem. Commun.* **2015**, 51, 17540-17543.
(24) Murnaghan, K. D.; Carbonera, C.; Toupet, L.; Griffin, M.; Dîrtu, M. M.; Desplanches, C.; Garcia, Y.; Collet, E.; Létard, J.-F.; Morgan, G. G. Spin-State Ordering on One Sub-lattice of a Mononuclear Iron(III) Spin Crossover Complex Exhibiting LIESST and TIESST. *Chem. Eur. J.* **2014**, *20*, 5613–5618.
(25) Griffin, M.; Shakespeare, S.; Shepherd, H. J.; Harding, C. J.; Létard, J.-F.; Desplanches, C.; Goeta, A. E.; Howard, J. A. K.; Powell, A. K.; Mereacre, V.; Garcia, Y.; Naik, A. D.; Müller-Bunz, H.; Morgan, G. G. A Symmetry-Breaking Spin-State Transition in Iron(III). *Angew. Chem. Int. Ed.* **2011**, *50*, 896–900.
(26) Fitzpatrick, A. J.; O'Connor, H. M.; Morgan, G. G. A room temperature spin crossover ionic liquid. *Dalton Trans.* **2015**, *44*, 20839-20842.

(27) Phonsri, W.; Lewis, B.A.I.; Jameson, G.N.L.; Murray, K.S. Double spin crossovers: A new double salt strategy to improve magnetic and memory properties. *Chem. Commun.* **2019**, *55*, 14031–14034.
(28) Phonsri, W.; Macedo, D.S.; Lewis, B.A.I.; Wain, D.F.; Murray, K.S. Iron(III) Azadiphenolate Compounds in a New Family of Spin Crossover Iron(II)–Iron(III) Mixed-Valent Complexes. *Magnetochemistry* **2019**, *5*, 37.
(29) Murata, S.; Takahashi, K.; Sakurai, T.; Ohta, H.; Yamamoto, T.; Einaga, Y.; Shiota, Y.; Yoshizawa, K. The Role of Coulomb Interactions for Spin Crossover Behaviors and Crystal Structural Transformation in Novel Anionic Fe(III) Complexes from a π-Extended ONO Ligand. *Crystals* **2016**, *6*, 49.
(30) Takahashi, K.; Kawamukai, K.; Okai, M.; Mochida, T.; Sakurai, T.; Ohta, H.; Yamamoto, T.; Einaga, Y.; Shiota, Y.; Yoshizawa, K. A New Family of Anionic Fe^{III} Spin Crossover Complexes Featuring a Weak-Field N_2O_4 Coordination Octahedron. *Chem. Eur. J.* **2016**, *22*, 1253–1257.
(31) Cook, C.; Habib, F.; Aharen, T.; Clérac, R.; Hu, A.; Murugesu, M. High-Temperature Spin Crossover Behavior in a Nitrogen-Rich Fe^{III} Based System. *Inorg. Chem.* **2013**, *52*, 1825–1831.
(32) Li, Z.-Y.; Dai, J.-W.; Shiota, Y.; Yoshizawa, K.; Kanegawa, S.; Sato, O. Multi-Step Spin Crossover Accompanied by Symmetry Breaking in an Fe^{III} Complex: Crystallographic Evidence and DFT Studies. *Chem. Eur. J.* **2013**, *19*, 12948-12952.
(33) Floquet, S.; Guillou, N.; Négrier, P.; Rivière, E.; Boillot, M.-L. The crystallographic phase transition for a ferric thiosemicarbazone spin crossover complex studied by X-ray powder diffraction. *New J. Chem.* **2006**, *30*, 1621–1627.
(34) Floquet, S.; Boillot, M.-L.; Rivière, E.; Varret, F.; Boukheddaden, K.; Morineau, D.; Négrier, P. Spin transition with a large thermal hysteresis near room temperature in a water solvate of an iron(III) thiosemicarbazone complex. *New J. Chem.* **2003**, *27*, 341–348
(35) Zelentsov, V. V. Review of the anionic Fe^{III} complexes from thsa and thpu ligands. *Sov. Sci. Rev. Sect. B* **1987**, *10*, 485-512.
(36) Karuppannan, S. K.; Martín-Rodríguez, A.; Ruiz, E.; Harding, P.; Harding, D. J.; Yu, X.; Tadich, A.; Cowie, B.; Qi, D.; Nijhuis, C. A. Room temperature conductance switching in a molecular iron(III) spin crossover junction, *Chem. Sci.* **2021**, *12*, 2381-2388.
(37) Halcrow, M. A. (ed.) *Spin-Crossover Materials: Properties and Applications* (Wiley, 2013).
(38) Kumar, K. S.; Ruben, M. Emerging trends in spin crossover (SCO) based functional materials and devices. *Coord. Chem. Rev.* **2017**, *346*, 176-205.
(39) Pittala, N.; Thétiot, F.; Triki, S.; Boukheddaden, K.; Chastanet, G.; Marchivie, M. Cooperative 1D Triazole-Based Spin Crossover Fe^{II} Material With Exceptional Mechanical Resilience. *Chem. Mater*. **2017**, *29*, 490–494.
(40) Phan, H.; Hrudka, J. J.; Igimbayeva, D.; Lawson Daku, L. M.; Shatruk, M. A Simple Approach for Predicting the Spin State of Homoleptic Fe(II) Tris-diimine Complexes. *J. Am. Chem. Soc.* **2017**, *139*, 6437-6447.

(41) Pittala, N.; Thétiot, F.; Charles, C.; Triki, S.; Boukheddaden, K.; Chastanet, G.; Marchivie, M. An unprecedented trinuclear Fe^{II} triazole-based complex exhibiting a concerted and complete sharp spin transition above room temperature. *Chem. Commun.* **2017**, *53*, 8356-8359.
(42) Milin, E.; Patinec, V.; Triki, S.; Bendeif, E.-E.; Pillet, S.; Marchivie, M.; Chastanet, G.; Boukheddaden, K. Elastic Frustration Triggering Photoinduced Hidden Hysteresis and Multistability in a Two-Dimensional Photoswitchable Hofmann-Like Spin-Crossover Metal-Organic Framework. *Inorg. Chem*. **2016**, *55*, 11652-11661.
(43) Shatruk, M.; Phan, H.; Chrisostomo, B. A.; Suleimenova, A. Symmetry-breaking structural phase transitions in spin crossover complexes. *Coord. Chem. Rev*. **2015**, *289-290*, 62-73.
(44) Atmani, C.; El Hajj, F.; Benmansour, S.; Marchivie, M.; Triki, S.; Conan, F.; Patinec, V.; Handel, H.; Dupouy, G.; Gómez-García, C. J. Guidelines to design new spin crossover materials. *Coord. Chem. Rev.* **2010**, *254*, 1559-1569.
(45) Yamada, M.; Ooidemizu, M.; Ikuta, Y.; Osa, S.; Matsumoto, N.; Iijima, S.; Kojima, M.; Dahan, F.; Tuchagues, J.-P. Interlayer Interaction of Two-Dimensional Layered Spin Crossover Complexes $[Fe^{II}H_3L^{Me}][Fe^{II}L^{Me}]X$ (X^- = ClO_4^-, BF_4^-, PF_6^-, AsF_6^-, and SbF_6^-; H_3L^{Me} = Tris[2-(((2-methylimidazol-4-yl)methylidene)amino)ethyl]amine). *Inorg. Chem.* **2003**, *42*, 8406-8416.
(46) Gómez, V.; Sáenz de Pipaón, C.; Maldonado-Illescas, P.; Waerenborgh, J.C.; Martin, E.; Benet-Buchholz, J.; Galán-Mascarós, J.-R. Easy Excited-State Trapping and Record High T_{TIESST} in a Spin-Crossover Polyanionic Fe(II) Trimer. *J. Am. Chem. Soc.* **2015**, *137*, 11924–11927.
(47) M. Klein, Y.; Sciortino, N. F.; Housecroft, C. E.; Kepert, C. J.; Neville, S. M. Structure and Magnetic Properties of the Spin Crossover Linear Trinuclear Complex $[Fe_3(furtrz)_6(ptol)_2(MeOH)_4]\cdot4(ptol)\cdot4(MeOH)$ (furtrz: furanylidene-4H-1,2,4-triazol-4-amine ptol: p-tolylsulfonate). *Magnetochemistry* **2016**, 2, 7.
(48) Savard, D.; Cook, C.; Enright, G. D.; Korobkov, I.; Burchell, T. J.; Murugesu, M. Gradual spin crossover behaviour in a linear trinuclear Fe^{II} complex. *Cryst. Eng. Commun.* **2011**, *13*, 5190-5197.
(49) Shakirova, O. G.; Lavrenova, L. G.; Shvedenkov, Y. G.; Berezovskii, G. A.; Naumanov, D. Y.; Sheludyakova, L. A.; Dolgushin, G. V.; Larionov, S. V. Synthesis and Physicochemical Study of Iron(II), Cobalt(II), Nickel(II), and Copper(II) Complexes with 4-(2-Pyridyl)-1,2,4-Triazole. *Russ. J. Coord. Chem.* **2004**, *30*, 473-479.
(50) Garcia, Y.; Guionneau, P.; Bravic, G.; Chasseau, D.; Howard, J. A. K.; Kahn, O.; Ksenofontov, V.; Reiman, S.; Gütlich, P. Synthesis, Crystal Structure, Magnetic Properties and ^{57}Fe Mössbauer Spectroscopy of the New Trinuclear $[Fe_3(4\text{-}(2'\text{-}hydroxyethyl)\text{-}1,2,4\text{-}triazole)_6\ (H_2O)_6](CF_3SO_3)_6$ Spin Crossover Compound. *Eur. J. Inorg. Chem.* **2000**, 1531-1538.
(51) Kolnaar, J. J. A.; van Dijk, G.; Koojiman, H.; Spek, A. L.; Ksenofontov, V.; Gütlich, P.; Haasnoot, J. G.; Reedijk, J. Synthesis, Structure, Magnetic Behavior, and Mössbauer Spectroscopy of Two New Iron(II) Spin-Transition Compounds with the

Ligand 4-Isopropyl-1,2,4-triazole. X-ray Structure of [Fe_3(4-isopropyl-1,2,4-triazole)$_6$(H_2O)$_6$](tosylate)$_6$·2H_2O. *Inorg. Chem.* **1997**, *36*, 2433-2440.
(52) Thomann, M.; Kahn, O.; Guilhem, J.; Varret, F. Spin Conversion versus Antiferromagnetic Interaction in Iron(II) Trinuclear Species. Crystal Structures and Magnetic Properties of [Fe_3(p-MeOptrz)$_6$(H_2O)$_4$](BF_4)$_6$ and [Fe_3(p-MeOptrz)$_6$(H_2O)$_6$](tos)$_6$ [p-MeOptrz = 4-*p*-Methoxyphenyl)-1,2,4-triazole, tos =Tosylate]. *Inorg. Chem.* **1994**, *33*, 6029-6037.
(53) Vos, G.; le Febre, R. A.; de Graaff, R. A. G.; Haasnoot, J. G.; Reedijk, J. Unique high-spin-low-spin transition of the central ion in a linear, trinuclear iron(II) triazole compound. *J. Am. Chem. Soc* **1983**, *105*, 1682-1683.
(54) Hirosawa, N.; Oso, Y.; Ishida, T. Spin crossover and light-induced excited spin-state trapping observed for an iron (II) complex chelated with tripodal tetrakis (2-pyridyl) methane. *Chem. Lett.* **2012**, *41*, 716-718.
(55) Yamasaki, M.; Ishida, T. Spin-crossover thermal hysteresis and light-induced effect on iron (II) complexes with tripodal tris (2-pyridyl) methanol. *Polyhedron* **2015**, *85*, 795-799.
(56) Yamasaki, M.; Ishida, T. Heating-rate dependence of spin-crossover hysteresis observed in an iron (II) complex having tris (2-pyridyl) methanol. *J. Mater. Chem. C* **2015**, *3*, 7784-7787.
(57) Ishida, T.; Kaneto, T.; Yamasaki, M. An iron(II) complex tripodally chelated with 1,1,1-tris(pyridine-2-yl)ethane showing room-temperature spin-crosssover behaviour. *Acta Cryst.* **2016**, *C72*, 797-801.
(58) Kashiro, A.; Some, K.; Kobayashi, Y.; Ishida, T. Iron(II) and 1,1,1-Tris(2-pyridyl)nonadecane Complex Showing an Order–Disorder-Type Structural Transition and Spin-Crossover Synchronized over Both Conformers. *Inorg. Chem.* **2019**, *58*, 7672-7676.
(59) Cuza, E.; Benmansour, S.; Cosquer, N.; Conan, F.; Pillet, S.; Gómez-García, C. J.; Triki, S. Spin Cross-Over (SCO) Anionic Fe(II) Complexes Based on the Tripodal Ligand Tris(2-pyridyl)ethoxymethane. *Magnetochemistry* **2020**, *6*, 26.
(60) Coronado, E.; Galán-Mascarós, J. R.; Gómez-García, C. J.; Laukhin, V. Coexistence of ferromagnetism and metallic conductivity in a molecule-based layered compound, *Nature* **2000**, *408*, 447–449.
(61) Kashiro, A.; Kohno, W.; Ishida, T. Odd−Even Effect on the Spin-Crossover Temperature in Iron(II) Complex Series Involving an Alkylated or Acyloxylated Tripodal Ligand. *Inorg. Chem.* **2020**, *59*, 10163–10171.
(62) Yamasaki, M.; Ishida, T. First Iron(II) Spin-crossover Complex with an N_5S Coordination Sphere. *Chem. Lett.* **2015**, *44*, 920-921.
(63) Mekuimemba, C. D.; Conan, F.; Mota, A. J.; Palacios, M. A.; Colacio, E.; Triki, S. On the Magnetic Coupling and Spin Crossover Behavior in Complexes Containing the Head-to-Tail [Fe^{II}_2(μ-SCN)$_2$] Bridging Unit: A Magnetostructural Experimental and Theoretical Study. *Inorg. Chem.* **2018**, *57*, 2184-2192.
(64) Nebbali, K.; Mekuimemba, C. D.; Charles, C.; Yefsah, S.; Chastanet, G.; Mota, A. J.; Colacio, E.; S. Triki, One-Dimensional Thiocyanato-Bridged Fe(II) Spin Crossover

Cooperative Polymer With Unusual FeN_5S Coordination Sphere. *Inorg. Chem.* **2018**, *57*, 12338-12346.
(65) Bernstein, J. Polymorphism - A Perspective. *Crystal Growth & Design* **2011**, *11*, 632-650**.**
(66) White, D. L.; Faller, J. W. Preparation and Reactions of the C_{3v} Ligand Tris(2-pyridyl)methane and Its Derivatives. *Inorg. Chem.* **1982**, *21*, 3119-3122.
(67) Jonas, R. T.; Stack, T. D. P. Synthesis and Characterization of a Family of Systematically Varied Tris(2-pyridyl)methoxymethane Ligands: Copper(I) and Copper(II) Complexes. *Inorg. Chem.* **1998**, *37*, 6615-6629.
(68) Chastanet, G.; Desplanches, C.; Baldé, C.; Rosa, P.; Marchivie, M.; Guionneau, P. A critical review of the T(LIESST) temperature in spin crossover materials – what it is and what it is not, *Chem. Sq.* **2018**, 2, 1-18.
(69) Bain, G. A.; Berry, J. F. Diamagnetic corrections and Pascal's constants. *J. Chem. Educ.* **2008**, *85*, 532-536.
(70) Guionneau, P.; Marchivie, M.; Bravic, G.; Létard, J.-F.; Chasseau, D. Structural Aspects of Spin Crossover. Example of the $[Fe^{II}L_n(NCS)_2]$ Complexes. *Top. Curr. Chem.* **2004**, *234*, 97–128.
(71) Baldé, C.; Desplanches, C.; Le Gac, F.; Guionneau, P.; Létard, J.-F. The role of iron(II) dilution in the magnetic and photomagnetic properties of the series $[Fe_xZn_{1-x}(bpp)_2](NCSe)_2$. *Dalton Trans.* **2014**, *43*, 7820–7829.
(72) Effect of Metal Dilution on the Thermal Spin Transition of $[Fe_xZn_{1-x}(bapbpy)(NCS)_2]$. Zheng, S.; Siegler, M. A.; Costa, J. S.; Fu, W.-T.; Bonnet, S. *Eur. J. Inorg. Chem.* **2013**, 1033–1042.
(73) Nakamoto, K. Infrared and Raman Spectra of Inorganic and Coordination Compounds - Part B: Applications in Coordination, Organometallic, and Bioinorganic Chemistry, Wiley, **2015**.
(74) Sorai, M.; Seki, S. Phonon coupled cooperative low-spin $^1A^1 \leftrightarrow$ high-spin $^5T_2$ transition in $[Fe(phen)_2(NCS)_2]$ and $[Fe(phen)_2(NCSe)_2]$ crystals. *J. Pbys. Chm. Solids* **1974**, *35*, 555-570.
(75) Brehm, G.; Reiher, M.; Le Guennic, B.; Leibold, M.; Schindler, S.; Heinemann, F. W.; Schneider, S. Investigation of the low-spin to high-spin transition in a novel $[Fe(pmea)(NCS)_2]$ complex by IR and Raman spectroscopy and DFT calculations. *J. Raman Spectrosc.* **2006**, *37,* 108-122.
(76) Park, Y.; Jung, Y. M.; Sarker, S.; Lee, J.-J.; Lee, Y.; Lee, K.; Oh, J. J.; Joo, S.-W. Temperature-dependent infrared spectrum of $(Bu_4N)_2[Ru(dcbpyH)_2(NCS)_2]$ on nanocrystalline TiO_2 surfaces. *Solar Energy Materials & Solar Cells* **2010**, *94*, 857–864.
(77) Varma,V.; Fernandes, J.-R. An Infrared Spectroscopic Study of the Low-Spin-High-spin transition in in $Fe_xMn_{1-x}(Phen)_2(NCS)_2$: a Composition-Induced Change in the Order of the Spin-State Transition. *Chem. Phys. Let.* **1990**, *167*, 367-370.
(78) Sankar, G.; Thomas, J. M.; Varma, V.; Kulkani, G. U.; Rao, C. N. R. An investigation of the first-order spin-state transition in the $Fe(Phen)_2(NCS)_2$ EXAFS and infrared spectroscopy. *Chem. Phys. Let.* **1996**, *251*, 79-83.

(79) Smit, E.; de Waal, D.; Heyns, A. M. The spin-transition complexes $[Fe(Htrz)_3](ClO_4)_2$ and $[Fe(NH_2trz)_3](ClO_4)_2$ I. FT-IR spectra of a low pressure and a low temperature phase transition, *Materials Research Bulletin* **2000**, *35*, 1697–1707.
(80) Durand, P.; Pillet, S.; Bendeif, E.-E.; Carteret, C.; Bouazaoui, M.; El Hamzaoui, H.; Capoen, B.; Salmon, L.; Hébert, S.; Ghanbaja, J.; Aranda, L.; Schaniel, D. Room temperature bistability with wide thermal hysteresis in a spin crossover silica nanocomposite. *J. Mater. Chem. C* **2013**, *1*,1933-1942.
(81) Naggert, H.; Bannwarth, A.; Chemnitz, S.; von Hofe, T.; Quandt, E.; F. Tuczek, F. First observation of light-induced spin change in vacuum deposited thin films of iron spin crossover complexes. *Dalton Trans.* **2011**, *40*, 6364-6366.
(82) Slimani, A.; Varret, F.; Boukheddaden, K.; Garrot, D.; Oubouchou, H.; Kaizaki, S. Velocity of the High-Spin Low-Spin Interface Inside the Thermal Hysteresis Loop of a Spin-Crossover Crystal, via Photothermal Control of the Interface Motion. *Phys. Rev. Lett*. **2013**, *110*, 087208.

For Table of Contents Only

A spin crossover (*SCO*) and a high spin (*HS*) Fe(II) anionic polymorph complexes have been described. Thermal evolutions of their spin states including the photo-induced effects have been analyzed using structural, magnetic and infrared spectroscopic investigations.